Comput Mech (2010) 45:227–243
DOI 10.1007/s00466-009-0434-z

ORIGINAL PAPER

Electromechanics of the heart: a unified approach to the strongly coupled excitation–contraction problem

Serdar Göktepe · Ellen Kuhl

Received: 9 July 2009 / Accepted: 14 October 2009 / Published online: 10 November 2009

Abstract This manuscript is concerned with a novel, unified finite element approach to fully coupled cardiac electromechanics. The intrinsic coupling arises from both the excitation-induced contraction of cardiac cells and the deformation-induced generation of current due to the opening of ion channels. In contrast to the existing numerical approaches suggested in the literature, which devise staggered algorithms through distinct numerical methods for the respective electrical and mechanical problems, we propose a fully implicit, entirely finite element-based modular approach. To this end, the governing differential equations that are coupled through constitutive equations are recast into the corresponding weak forms through the conventional isoparametric Galerkin method. The resultant non-linear weighted residual terms are then consistently linearized. The system of coupled algebraic equations obtained through discretization is solved monolithically. The put-forward modular algorithmic setting leads to an unconditionally stable and geometrically flexible framework that lays a firm foundation for the extension of constitutive equations towards more complex ionic models of cardiac electrophysiology and the strain energy functions of cardiac mechanics. The performance of the proposed approach is demonstrated through three-dimensional illustrative initial boundary-value problems that include a coupled electromechanical analysis of a biventricular generic heart model.

Keywords Coupled problems · Cardiac electromechanics · Excitation–contraction · Finite elements

S. Göktepe (✉) · E. Kuhl
Departments of Mechanical Engineering and Bioengineering,
Stanford University, Stanford, CA 94305, USA
e-mail: goktepe@stanford.edu

E. Kuhl
e-mail: ekuhl@stanford.edu

1 Introduction

Heart disease is the primary threat to human life in developed countries. In the United States, for example, half a million people yearly die because of heart diseases such as cardiac arrhythmias [44]. Recent research in medicine and bioengineering striving for the treatment of infarcted cardiac tissue advocates stem cell-based therapies. Undoubtedly, computational models of cardiac electromechanics are powerful tools, used to guide a successful patient specific therapy design. They do not only play a crucial role in reproducing biological cardiac behavior by incorporating experimental findings but also serve as a virtual testing environment for predictive analyses where experimental techniques fall short [14,31]. The predictive quality of the computational tools crucially hinges on physiologically well-founded, detailed constitutive models and on their robust, efficient and stable algorithmic implementation. Therefore, it is the key objective of this work to develop an efficient, robust, modular, and unified finite element approach to the fully coupled cardiac electromechanical problem. In the remainder of this section, we provide an introduction to computational cardiac electromechanics in a nutshell. Hence, an exhaustive review of the existing literature is not aimed; instead, only a few selected references are addressed.

The heart is mainly made of contractile muscle cells, myocytes, that constitute approximately 75% of the solid heart volume. Myocytes have a cylindrical shape, range from 10 to 25 μm in diameter and can reach up to 100 μm in length. The rest of the heart consists of pacemaker cells, conducting tissue, blood vessels and extracellular media [15,28]. The myocardium possesses a hierarchical micro-structure where myocytes are arranged in bundles of myofibers. These fibers wind around the heart in an organized way, thereby resulting in highly anisotropic and heterogeneous architecture.

Directional orientation of the myofibers is relatively well documented in the literature [26,32,36]. Roughly speaking, the orientation of myofibers exhibits a left-handed spiral-like pattern in the epicardium (outer wall) and a right-handed spiral-like arrangement in the endocardium (inner wall). Variation of the fiber orientation across the heart wall is fairly smooth. This arrangement of myofibers is of vital importance for the successful transduction of essentially one-dimensional contraction of myocytes to the overall pumping function of the heart.

On the lower scale of the hierarchical micro-structure, myocytes contain bundles of contractile myofibrils that are formed by sarcomeres, the basic contractile unit. Sarcomeres, which measure about 2 μm in length, are connected in series to form myofibrils. Two major protein molecules of sarcomeres, thick myosin and thin actin, slide over each other, thereby pulling the two ends (Z-lines) of the sarcomere. The entire complex process, called cross-bridging, is where the myosin heads interact with the binding side of the actin filaments. Cross-bridging is triggered by calcium influx [3] upon rapid depolarization of the myocyte from the polarized resting state with transmembrane potential of $\Phi \approx -80$ mV to the depolarized state with $\Phi \approx +20$ mV. From the depolarized state, the myocyte repolarizes back to its resting state through complex ion in- and efflux dynamics across the cell membrane. The depolarization, also referred to as excitation, and repolarization result in the action potentials, Fig. 4, whose characteristics are intrinsic to different kinds of excitable cardiac cells. The electrical depolarization activity of the heart is initiated at its natural pacemaker, the sinoatrial node, located in the right atrium. The depolarization wave travels through the atria, the upper chambers of the heart, and is then conducted to the ventricles, the lower chambers, via a special conducting system involving the atrioventicular node, left and right bundle branches, Purkinje fibers, and the myocardium. The generation and propagation of excitation waves are controlled by opening and closing of ion channels in the cell membrane. Apart from the excitation-induced depolarization and contraction of cardiac cells, myocytes can also be excited through the stretch-induced opening of ion channels, commonly referred to as the mechano-electric feedback [16]. This phenomenon is considered to be extremely crucial to understand the interplay between electrophysiology and mechanics of myocytes, especially regarding the transient pacemaker organization and fibrillation [13]. Therefore, it is of fundamental importance that a complete computational modeling approach to cardiac electromechanics accounts not only for the excitation-triggered contraction of myocytes but also for the stretch-activated excitation of cardiac cells.

Quantitative modeling of electrophysiology of cells can be traced back to the seminal work of Hodgkin and Huxley [10] on neural cells. About a decade later, their celebrated four-parameter model was considerably simplified by FitzHugh [7] and Nagumo et al. [20] to a two-parameter phenomenological model involving only two ordinary differential equations for the rapidly evolving transmembrane potential Φ and the recovery variable r that evolves slower than Φ. This pioneering work has then been followed by the action potential models of cardiac cells proposed by Noble [27], Beeler and Reuter [2], Luo and Rudy [18], to mention a few. We also refer to the recent literature [4,6,12,33,37,41] for excellent classifications of the cardiac cell models. To describe the spatial propagation of excitations waves (depolarization front), the local cell models have been extended to the reaction–diffusion-type formulations through a phenomenological conduction term. In this context, Aliev and Panfilov [1] and Fenton and Karma [5] suggested the numerical analysis of traveling excitation waves with the help of explicit finite difference schemes. At the same time, one of the first finite element algorithms for cardiac action potential propagation was suggested by Rogers and McCulloch [34,35]. In our recent work on computational cardiac electrophysiology [8], we proposed a new, algorithmically efficient, fully implicit finite element approach based on the global–local split of the fast and slow variables. We have successfully applied this method to three-dimensional fibrillation simulations [9] and to patient-specific calculation of electrocardiograms [17]. The formulation proposed in this paper extends this approach to the fully coupled electromechanics of the heart where both the excitation-induced contraction of myocytes and the deformation-activated ion channels play an important role.

Apart from the approaches to computational rigid cardiac electrophysiology, mentioned above, and models dealing with purely mechanical passive behavior of the heart [11,21], there have also been attempts aimed at incorporating the mechanical field through excitation–contraction coupling. However, most existing algorithms are based on a staggered time stepping scheme that combines a finite difference approach to integrate the excitation equations through an explicit forward Euler algorithm with a finite element approach for the mechanical equilibrium problem [13,22,23,29]. Therefore, they require sophisticated mappings from a fine electrical grid to a coarser mechanical mesh to map the potential field, and vice versa, the deformation field. In this line, the methods suggested, for example in [24,38,42] among others, devise operator splitting schemes for the solution of the coupled problem. It, however, is a well known fact that these algorithms have drawbacks regarding the numerical stability. They are only conditionally stable [25], and thus, the size of the time step is restricted to extremely small values. Moreover, the latter approaches are only one-way coupled, neglecting the mechano-electric feedback.

In contrast to the existing numerical approaches in the literature; to the best of our knowledge, we, for the first time, propose a fully implicit, entirely finite-element-based approach to the strongly coupled non-linear problem of

cardiac electromechanics. Accordingly, the governing differential equations that are coupled through constitutive equations are recast into the corresponding weak forms through the conventional isoparametric Galerkin method. The resultant non-linear weighted residual terms are then consistently linearized in the Eulerian setting. The system of coupled algebraic equations obtained through discretization is solved simultaneously. This results in an unconditionally stable, modular and geometrically flexible structure. The put forward framework accounts for both the excitation-induced contraction of cardiac tissue and the deformation-induced generation of current due to the opening of ion channels. The suggested algorithmic setting is tailored in such a general way that it can readily be furthered towards physiologically more complex ionic models of cardiac electrophysiology where the concentration of ions directly enters the formulation. We illustrate the performance of the proposed approach by means of three-dimensional representative initial boundary-value problems that cover the re-entrant scroll dynamics and impact loading-generated excitation in a slice of contractile cardiac tissue and the coupled electromechanical analysis of a biventricular generic heart model.

The paper is organized as follows. In Sect. 2, we introduce the governing equations of a coupled initial boundary-value problem of cardiac electromechanics. Section 3 is devoted to the derivation of the weak forms of the field equations, their linearization, and their spatio-temporal discretization. In Sect. 4, we consider a model problem of cardiac electromechanics where the specific constitutive equations are described and the associated consistent algorithmic tangents are derived. Section 5 is concerned with several numerical examples demonstrating the distinctive performance of the proposed approach. We conclude the manuscript with some closing remarks in Sect. 6.

2 Field equations of cardiac electromechanics

In this section, we introduce the fundamental equations of the coupled boundary-value problem of cardiac electromechanics. After briefly introducing the key geometric maps of non-linear continuum mechanics, we present two essential differential equations of the coupled problem along with the corresponding boundary conditions. Apart from the kinematic and field equations, the specific functional dependencies of constitutive equations are outlined to address the intrinsically coupled electromechanical character of the problem of interest.

2.1 Kinematics

Let $\mathcal{B} \subset \mathbb{R}^3$ be the reference configuration of an excitable and deformable solid body that occupies the current configuration

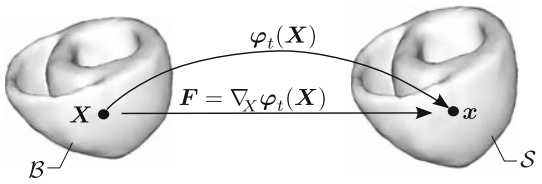

Fig. 1 Motion of an excitable and deformable solid body in the Euclidean space $\mathbb{R}^3$ through the non-linear deformation map $\boldsymbol{\varphi}_t(\boldsymbol{X})$ at time t. The deformation gradient $\boldsymbol{F} = \nabla_{\boldsymbol{X}} \boldsymbol{\varphi}_t(\boldsymbol{X})$ describes the tangent map between the respective tangent spaces

$\mathcal{S} \subset \mathbb{R}^3$ at time $t \in \mathbb{R}_+$ as shown Fig. 1. Material points $\boldsymbol{X} \in \mathcal{B}$ are mapped onto their spatial positions $\boldsymbol{x} \in \mathcal{S}$ through the non-linear deformation map $\boldsymbol{x} = \boldsymbol{\varphi}_t(\boldsymbol{X}) : \mathcal{B} \to \mathcal{S}$ at time t. The deformation gradient $\boldsymbol{F} := \nabla_{\boldsymbol{X}} \boldsymbol{\varphi}_t(\boldsymbol{X}) : T_{\boldsymbol{X}}\mathcal{B} \to T_{\boldsymbol{x}}\mathcal{S}$ acts as the tangent map between the tangent spaces of the respective configurations. The gradient operator $\nabla_{\boldsymbol{X}}[\bullet]$ denotes the spatial derivative with respect to the reference coordinates $\boldsymbol{X}$. Moreover, the Jacobian $J := \det \boldsymbol{F} > 0$ describes the volume map of the infinitesimal reference volume elements onto the associated spatial volume elements. Furthermore, the reference $\mathcal{B}$ and the spatial $\mathcal{S}$ manifolds are locally furnished with the reference $\boldsymbol{G}$ and current $\boldsymbol{g}$ metric tensors in the neighborhoods $\mathcal{N}_{\boldsymbol{X}}$ of $\boldsymbol{X}$ and $\mathcal{N}_{\boldsymbol{x}}$ of $\boldsymbol{x}$, respectively. These metric tensors are required for calculating basic deformation measures such as stretches, angle changes, and invariants.

2.2 Governing differential equations

A coupled problem of cardiac electromechanics is formulated in terms of the two primary field variables, namely the placement $\boldsymbol{\varphi}(\boldsymbol{X}, t)$ and the action potential $\Phi(\boldsymbol{X}, t)$. The former has already been introduced above in Fig. 1. The latter refers to a potential difference between the intracellular domain and the extracellular domain within the context of mono-domain formulations of cardiac electrophysiology [8,12,22]. An electromechanical state of a material point $\boldsymbol{X}$ at time t is then defined by

$$\text{State}(\boldsymbol{X}, t) := \{\boldsymbol{\varphi}(\boldsymbol{X}, t),\ \Phi(\boldsymbol{X}, t)\}\,. \tag{1}$$

Spatial and temporal evolution of the primary field variables are governed by two basic field equations, namely the balance of linear momentum and the reaction–diffusion-type equation of excitation.

The balance of linear momentum that assumes the following well-known local spatial form

$$J\,\text{div}[J^{-1}\hat{\boldsymbol{\tau}}] + \boldsymbol{B} = \boldsymbol{0} \quad \text{in } \mathcal{B} \tag{2}$$

describes the quasi-static stress equilibrium in terms of the Eulerian Kirchhoff stress tensor $\hat{\boldsymbol{\tau}}$ and a given body force $\boldsymbol{B}$ per unit reference volume. The operator $\text{div}[\bullet]$ denotes the divergence with respect to spatial coordinates $\boldsymbol{x}$. Note that

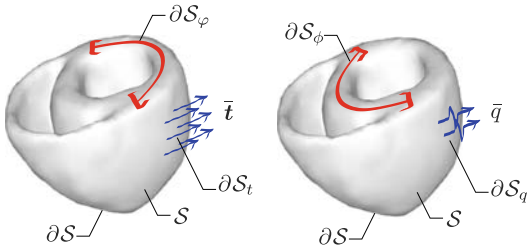

Fig. 2 Depiction of the mechanical (*left*) and electrophysiological (*right*) natural and essential boundary conditions

the momentum balance depends non-linearly on the primary field variables through the Kirchhoff stress tensor $\hat{\boldsymbol{\tau}}$, whose specific form is elaborated in the forthcoming subsection. The essential and natural boundary conditions, Fig. 2 (left),

$$\boldsymbol{\varphi} = \bar{\boldsymbol{\varphi}} \quad \text{on } \partial\mathcal{S}_\varphi \quad \text{and} \quad \boldsymbol{t} = \bar{\boldsymbol{t}} \quad \text{on } \partial\mathcal{S}_t, \tag{3}$$

complete the description of the mechanical problem. The union of the surface subdomains, on which the boundary conditions (3) are prescribed, forms the total spatial surface $\partial\mathcal{S} = \partial\mathcal{S}_\varphi \cup \partial\mathcal{S}_t$ where $\partial\mathcal{S}_\varphi$ and $\partial\mathcal{S}_t$ are disjoint, i.e. $\partial\mathcal{S}_\varphi \cap \partial\mathcal{S}_t = \emptyset$. The surface stress traction vector $\bar{\boldsymbol{t}}$, defined on $\partial\mathcal{S}_t$, is related to the Cauchy stress tensor through the Cauchy stress theorem $\bar{\boldsymbol{t}} := J^{-1}\boldsymbol{\tau} \cdot \boldsymbol{n}$ where $\boldsymbol{n}$ denotes the outward surface normal on $\partial\mathcal{S}$.

The second field equation of the coupled problem that falls into the class of mono-domain formulations of electrophysiology is commonly referred to as the FitzHugh–Nagumo-type model due to the seminal works of FitzHugh [7] and Nagumo et al. [20].

The phenomenological excitation equation of the following form

$$\dot{\Phi} - J\,\mathrm{div}[J^{-1}\hat{\boldsymbol{q}}] - \hat{F}^\phi = 0 \quad \text{in } \mathcal{B} \tag{4}$$

describes the spatio-temporal evolution of the action potential field $\Phi(\boldsymbol{X}, t)$ in terms of the diffusion term $\mathrm{div}[J^{-1}\hat{\boldsymbol{q}}]$ and the non-linear current term $\hat{F}^\phi$. Henceforth, we employ the notation $[\dot{\bullet}] := \mathrm{D}[\bullet]/\mathrm{D}t$ to denote the material time derivative. In cardiac electrophysiology, the source term $\hat{F}^\phi$ plays a key role in determining the excitability and oscillatory nature of cells. In particular, it governs whether the excitation model exhibits the self-oscillatory pacemaker behavior or the non-oscillatory excitable cell behavior [8,12]. The current source $\hat{F}^\phi$ also controls characteristics of the action potential regarding its shape, duration, restitution, and hyperpolarization along with another variable, the so-called recovery variable r whose evolution is governed by an additional ordinary differential equation. Since the recovery variable r chiefly controls the local repolarization behavior of the action potential, we treat it as a local internal variable in our formulation. This will be more transparent as we introduce the explicit functional form of $\hat{F}^\phi$ and set out the algorithmic setting of the formulation. Analogous to the momentum balance, the Fitzhugh–Nagumo-type field equation of excitation is also furnished by the corresponding essential and natural boundary conditions, Fig. 2 (right),

$$\Phi = \bar{\Phi} \quad \text{on } \partial\mathcal{S}_\phi \quad \text{and} \quad q = \bar{q} \quad \text{on } \partial\mathcal{S}_q, \tag{5}$$

respectively. Note that the surface subdomains $\partial\mathcal{S}_\phi$ and $\partial\mathcal{S}_q$ are disjoint, $\partial\mathcal{S}_\phi \cap \partial\mathcal{S}_q = \emptyset$, and complementary, $\partial\mathcal{S} = \partial\mathcal{S}_\phi \cup \partial\mathcal{S}_t$. The electrical surface flux term $\bar{q}$ in $(5)_2$ is related to the spatial flux vector through the Cauchy-type formula $\bar{q} := J^{-1}\hat{\boldsymbol{q}} \cdot \boldsymbol{n}$ in terms of the spatial surface normal $\boldsymbol{n}$. Owing to the transient term in the excitation equation (4), its solution requires the knowledge of initial potential field at $t = t_0$

$$\Phi_0(\boldsymbol{X}) = \Phi(\boldsymbol{X}, t_0) \quad \text{in } \mathcal{B}. \tag{6}$$

Note that the "hat" sign used along with the terms $\hat{\boldsymbol{\tau}}$, $\hat{\boldsymbol{q}}$ and $\hat{F}^\phi$ indicates that these variables are dependent on the primary fields through constitutive equations, which we introduce next.

2.3 Constitutive equations

The two field equations along with the corresponding boundary and initial conditions introduced in the preceding subsection complete the strong description of a coupled boundary-value problem of cardiac electromechanics. The solution of the problem at hand, however, necessitates the knowledge of constitutive equations describing the Kirchhoff stress tensor $\hat{\boldsymbol{\tau}}$, the potential flux $\hat{\boldsymbol{q}}$, and the current source $\hat{F}^\phi$ appearing in (2) and (4).

As suggested in the literature, see e.g. [22,38], the Kirchhoff stress tensor $\hat{\boldsymbol{\tau}}$ is assumed to be composed of the passive $\hat{\boldsymbol{\tau}}^{\mathrm{pas}}$ and active $\hat{\boldsymbol{\tau}}^{\mathrm{act}}$ parts

$$\hat{\boldsymbol{\tau}} = \hat{\boldsymbol{\tau}}^{\mathrm{pas}}(\boldsymbol{g}; \boldsymbol{F}) + \hat{\boldsymbol{\tau}}^{\mathrm{act}}(\boldsymbol{g}; \boldsymbol{F}, \Phi). \tag{7}$$

The passive part $\hat{\boldsymbol{\tau}}^{\mathrm{pas}}$ is solely governed by mechanical deformation, while the active part $\hat{\boldsymbol{\tau}}^{\mathrm{act}}$ is generated by excitation-induced contraction of myocytes during the course of depolarization. Since the formulation is laid out in the Eulerian setting, we need to explicitly include the current metric $\boldsymbol{g}$ among the arguments of the constitutive functions.

The potential flux $\hat{\boldsymbol{q}}$ is assumed to depend linearly on the spatial potential gradient $\nabla_x \Phi$

$$\hat{\boldsymbol{q}} = \boldsymbol{D}(\boldsymbol{g}; \boldsymbol{F}) \cdot \nabla_x \Phi \tag{8}$$

through the deformation-dependent anisotropic spatial conduction tensor $\boldsymbol{D}(\boldsymbol{g}; \boldsymbol{F})$ that governs the conduction speed of the non-planar depolarization front in three-dimensional anisotropic cardiac tissue.

The last constitutive relation describes the electrical source term of the Fitzhugh–Nagumo-type excitation equation (4)

$$\hat{F}^{\phi} = \hat{F}^{\phi}_{\mathrm{e}}(\Phi, r) + \hat{F}^{\phi}_{\mathrm{m}}(\boldsymbol{g}; \boldsymbol{F}, \Phi) \tag{9}$$

that is additively decomposed into the excitation-induced purely electrical part $\hat{F}^{\phi}_{\mathrm{e}}(\Phi, r)$ and the stretch-induced mechano-electrical part $\hat{F}^{\phi}_{\mathrm{m}}(\boldsymbol{g}; \boldsymbol{F}, \Phi)$. The former describes the effective current generation due to the inward and outward flow of ions across the cell membrane. This ionic flow is triggered by a perturbation of the resting potential of a cardiac cell beyond some physical threshold upon the arrival of the depolarization front. The latter, on the other hand, incorporates the opening of ion channels under the action of deformation [16,22].

Note that apart from the primary field variables, as we briefly introduced in the preceding subsection, the recovery variable r appears among the arguments of $\hat{F}^{\phi}_{\mathrm{e}}$ in (9). It describes the repolarization response of the action potential. Evolution of the recovery variable r chiefly determines the shape and duration of the action potential locally inherent to each cardiac cell and may change throughout the heart. For this reason, evolution of the recovery variable r is commonly modeled by a local ordinary differential equation

$$\dot{r} = \hat{f}^{r}(\Phi, r). \tag{10}$$

From an algorithmic point of view, the local nature of the evolution equation (10) allows us to treat the recovery variable as an internal variable. This is one of the key features of the proposed formulation that preserves the modular global structure of the field equations as set out in our recent work [8]. Furthermore, as mentioned in Sect. 1, cardiac tissue possesses an anisotropic and inhomogeneous micro-structure. This undoubtedly necessitates the explicit incorporation of position-dependent orientation of myocytes, possibly in terms of structural tensors, in the argument list of the constitutive functions for $\hat{\boldsymbol{\tau}}$, $\hat{\boldsymbol{D}}$ and $\hat{F}^{\phi}_{m}$. At this stage, however, we have suppressed this dependency for the sake of conciseness by leaving details out until Sect. 4 where we introduce a model problem.

Having the field equations and the functional forms of the constitutive equations at hand, we are now in a position to construct a unified finite element framework for the monolithic numerical solution of the strongly coupled problem of cardiac electromechanics.

3 Finite element formulation

This section is devoted to the construction and consistent linearization of weak integral forms of the local non-linear field equations (2) and (4) introduced in the preceding section. For this purpose, we employ conventional isoparametric spatial discretization for the placement $\boldsymbol{\varphi}(\boldsymbol{X}, t)$ and potential $\Phi(\boldsymbol{X}, t)$ fields to transform the continuous integral equations for the non-linear weighted residual and for the Newton-type update to a set of coupled, discrete algebraic equations. This set of algebraic equations is then solved monolithically in an iterative manner for the nodal degrees of freedom.

3.1 Weak formulation

We follow the conventional Galerkin procedure to construct the weak forms of the governing field equations (2) and (4). To this end, we multiply the residual equations by the square-integrable weight functions $\delta\boldsymbol{\varphi} \in \mathscr{U}_0$ and $\delta\Phi \in \mathscr{V}_0$ that satisfy the essential boundary conditions (3) and (5) such that $\delta\boldsymbol{\varphi} = \boldsymbol{0}$ on $\partial\mathcal{S}_{\varphi}$ and $\delta\Phi = 0$ on $\partial\mathcal{S}_{\phi}$. We then integrate the weighted residual equations over the solid volume, and carry out integration by parts to obtain the following weighted residual expressions for the balance of linear momentum (2)

$$G^{\varphi}(\delta\boldsymbol{\varphi}, \boldsymbol{\varphi}, \Phi) = G^{\varphi}_{\mathrm{int}}(\delta\boldsymbol{\varphi}, \boldsymbol{\varphi}, \Phi) - G^{\varphi}_{\mathrm{ext}}(\delta\boldsymbol{\varphi}) = 0 \tag{11}$$

and for the FitzHugh–Nagumo-type equation (4)

$$G^{\phi}(\delta\Phi, \boldsymbol{\varphi}, \Phi) = G^{\phi}_{\mathrm{int}}(\delta\Phi, \boldsymbol{\varphi}, \Phi) - G^{\phi}_{\mathrm{ext}}(\delta\Phi, \boldsymbol{\varphi}, \Phi) = 0, \tag{12}$$

respectively. Explicit forms of the internal $G^{\varphi}_{\mathrm{int}}$ and external $G^{\varphi}_{\mathrm{ext}}$ terms in (11) are separately defined as

$$\begin{aligned} G^{\varphi}_{\mathrm{int}}(\delta\boldsymbol{\varphi}, \boldsymbol{\varphi}, \Phi) &:= \int_{\mathcal{B}} \nabla_x(\delta\boldsymbol{\varphi}) : \hat{\boldsymbol{\tau}}\, dV, \\ G^{\varphi}_{\mathrm{ext}}(\delta\boldsymbol{\varphi}) &:= \int_{\mathcal{B}} \delta\boldsymbol{\varphi} \cdot \boldsymbol{B}\, dV + \int_{\partial\mathcal{S}_t} \delta\boldsymbol{\varphi} \cdot \bar{\boldsymbol{t}}\, da, \end{aligned} \tag{13}$$

where the body force $\boldsymbol{B}$ and the surface traction $\bar{\boldsymbol{t}}$ are assumed to be given. Likewise, we obtain the following expressions for G^{ϕ}_{int} and G^{ϕ}_{ext}

$$\begin{aligned} G^{\phi}_{\mathrm{int}}(\delta\Phi, \boldsymbol{\varphi}, \Phi) &:= \int_{\mathcal{B}} (\delta\Phi\ \dot{\Phi} + \nabla_x(\delta\Phi) \cdot \hat{\boldsymbol{q}})\, dV, \\ G^{\phi}_{\mathrm{ext}}(\delta\Phi, \boldsymbol{\varphi}, \phi) &:= \int_{\mathcal{B}} \delta\Phi\ \hat{F}^{\phi} dV + \int_{\partial\mathcal{S}_q} \delta\Phi\ \bar{q} da, \end{aligned} \tag{14}$$

respectively. The surface flux $\bar{q}$ is prescribed as a natural boundary condition through $(5)_2$. Observe that, in contrast to the mechanical external term in $(13)_2$, G^{ϕ}_{ext} depends explicitly upon the field variables due to the non-linear source term $\hat{F}^{\phi}$ introduced in (9).

Before proceeding with the consistent linearization of the weak forms, it is convenient to introduce the discretization of the time space $\mathcal{T} := [0, t]$. For this purpose, we divide up the time interval $\mathcal{T}$ into n_{stp} divisions such that $\mathcal{T} = \bigcup_{n=0}^{n_{\mathrm{stp}}-1} [t_n, t_{n+1}]$. The current time step is denoted with $\Delta t := t - t_n$ where we have suppressed the subscript "$n+1$"

for the sake of compactness. Having the temporal discretization defined, we use the implicit Euler scheme to compute the time derivative of the potential Φ at time t

$$\dot{\Phi} \approx (\Phi - \Phi_n)/\Delta t \tag{15}$$

with $\Phi_n := \Phi(\boldsymbol{X}, t_n)$. Substitution of this finite difference approximation for $\dot{\Phi}$ into $(14)_1$ yields the following algorithmic form

$$G^{\phi,\text{algo}}_{\text{int}}(\delta\Phi, \boldsymbol{\varphi}, \Phi) = \int_{\mathcal{B}} (\, \delta\Phi \, \frac{\Phi - \Phi_n}{\Delta t} + \nabla_x(\delta\Phi) \cdot \hat{\boldsymbol{q}} \,)\, dV. \tag{16}$$

With the weak forms of the field equations at hand, we can then go on to carry out the consistent linearization.

Remark 1 Since the primary focus of the present formulation is the numerical treatment of the strongly coupled cardiac electromechanics; in the weak formulation of the mechanical part G^{φ} of the coupled problem, we restrict ourselves solely to the displacement approximation. Nevertheless, a possible extension of the present mechanical setting toward the well-established three-field (pressure-dilatation-displacement) finite element formulation along with the isochoric–volumetric decomposition of the deformation gradient can readily be carried out if quasi-incompressibility needs to be accounted for. The incompressibility of myocardium, on the other hand, seems to be a rather controversial issue due to the vascular network that constitutes 10–20% of the total volume of the ventricular wall. According to the experimental results reported by Yin et al. [43], for example, the changes in wall volume range between 5 and 10% due to the intravascular blood flow.

3.2 Consistent algorithmic linearization

The weighted residual equations (11) and (12) are non-linear functions of the field variables due to the spatial gradient operators and the non-linear constitutive equations. Therefore, simultaneous treatment of these equations necessitates utilization of Newton-type iterative solution schemes within the framework of the implicit finite element method. Accordingly, we carry out the consistent linearization of the weighted residuals with respect to the field variables at an intermediate iteration step at which the field variables assume the respective values $\tilde{\boldsymbol{\varphi}}$ and $\tilde{\Phi}$ to obtain:

$$\begin{aligned}
\text{Lin}\, G^{\varphi}(\delta\boldsymbol{\varphi}, \boldsymbol{\varphi}, \Phi)\big|_{\tilde{\boldsymbol{\varphi}},\tilde{\Phi}} &:= G^{\varphi}(\delta\boldsymbol{\varphi}, \tilde{\boldsymbol{\varphi}}, \tilde{\Phi}) \\
&\quad + \Delta G^{\varphi}(\delta\boldsymbol{\varphi}, \tilde{\boldsymbol{\varphi}}, \tilde{\Phi}; \Delta\boldsymbol{\varphi}, \Delta\Phi) = 0\,, \\
\text{Lin}\, G^{\phi}(\delta\Phi, \boldsymbol{\varphi}, \Phi)\big|_{\tilde{\boldsymbol{\varphi}},\tilde{\Phi}} &:= G^{\phi}(\delta\Phi, \tilde{\boldsymbol{\varphi}}, \tilde{\Phi}) \\
&\quad + \Delta G^{\phi}(\delta\Phi, \tilde{\boldsymbol{\varphi}}, \tilde{\Phi}; \Delta\boldsymbol{\varphi}, \Delta\Phi) = 0.
\end{aligned} \tag{17}$$

The incremental terms ΔG^{φ} and ΔG^{ϕ}, which can be obtained through the Gâteaux derivative, may be expressed in the following decomposed form

$$\Delta G^{\gamma} = \Delta G^{\gamma}_{\text{int}} - \Delta G^{\gamma}_{\text{ext}} \quad \text{for } \gamma = \varphi, \phi, \tag{18}$$

based on the definitions in (11) and (12). We then start with the elaboration of the increment $\Delta G^{\varphi}_{\text{int}}$ according to $(13)_1$

$$\Delta G^{\varphi}_{\text{int}} = \int_{\mathcal{B}} \Delta(\nabla_x(\delta\boldsymbol{\varphi})) : \hat{\boldsymbol{\tau}} + \nabla_x(\delta\boldsymbol{\varphi}) : \Delta\hat{\boldsymbol{\tau}}\, dV. \tag{19}$$

Linearization of the non-linear terms in (19) yields

$$\Delta(\nabla_x(\delta\boldsymbol{\varphi})) = -\nabla_x(\delta\boldsymbol{\varphi})\, \nabla_x(\Delta\boldsymbol{\varphi})\,, \tag{20}$$

$$\Delta\hat{\boldsymbol{\tau}} = \pounds_{\Delta\boldsymbol{\varphi}}\hat{\boldsymbol{\tau}} + \nabla_x(\Delta\boldsymbol{\varphi})\, \hat{\boldsymbol{\tau}} + \hat{\boldsymbol{\tau}}\, \nabla_x^T(\Delta\boldsymbol{\varphi}) + \boldsymbol{C}^{\varphi\phi}\Delta\Phi, \tag{21}$$

where $\pounds_{\Delta\boldsymbol{\varphi}}\hat{\boldsymbol{\tau}}$ denotes the objective Lie derivative along the increment $\Delta\boldsymbol{\varphi}$ and can be expressed as

$$\pounds_{\Delta\boldsymbol{\varphi}}\hat{\boldsymbol{\tau}} = \mathbb{C}^{\varphi\varphi} : \tfrac{1}{2}\pounds_{\Delta\boldsymbol{\varphi}}\boldsymbol{g} = \mathbb{C}^{\varphi\varphi} : (\boldsymbol{g}\nabla_x(\Delta\boldsymbol{\varphi})). \tag{22}$$

in terms of the Lie derivative of the current metric

$$\pounds_{\Delta\boldsymbol{\varphi}}\boldsymbol{g} = \boldsymbol{g}\, \nabla_x(\Delta\boldsymbol{\varphi}) + \nabla_x^T(\Delta\boldsymbol{\varphi})\, \boldsymbol{g}. \tag{23}$$

The fourth-order spatial tangent moduli $\mathbb{C}^{\varphi\varphi}$ in (22) and the sensitivity of the Kirchhoff stresses to the action potential $\boldsymbol{C}^{\varphi\phi}$ introduced in (21) are defined as

$$\mathbb{C}^{\varphi\varphi} := 2\partial_{\boldsymbol{g}}\hat{\boldsymbol{\tau}}(\boldsymbol{g}; \boldsymbol{F}, \Phi) \quad \text{and} \quad \boldsymbol{C}^{\varphi\phi} := \partial_{\Phi}\hat{\boldsymbol{\tau}}(\boldsymbol{g}; \boldsymbol{F}, \Phi), \tag{24}$$

respectively. Incorporation of the results (20) and (21) along with (22)–(24) in (19) results in the following well-known expression

$$\begin{aligned}
\Delta G^{\varphi}_{\text{int}} &= \int_{\mathcal{B}} \nabla_x(\delta\boldsymbol{\varphi}) : \mathbb{C}^{\varphi\varphi} : (\boldsymbol{g}\nabla_x(\Delta\boldsymbol{\varphi}))dV \\
&\quad + \int_{\mathcal{B}} \nabla_x(\delta\boldsymbol{\varphi}) : (\nabla_x(\Delta\boldsymbol{\varphi})\hat{\boldsymbol{\tau}})dV \\
&\quad + \int_{\mathcal{B}} \nabla_x(\delta\boldsymbol{\varphi}) : \boldsymbol{C}^{\varphi\phi}\Delta\Phi dV.
\end{aligned} \tag{25}$$

The three terms on the right-hand side of (25) clearly demonstrate the inherent nonlinearities arising from the entirely mechanical material response, from the geometry, and from the coupled electromechanical stress response. Since the body force $\boldsymbol{B}$ and the traction boundary conditions $\bar{\boldsymbol{t}}$ in $(13)_2$ are prescribed, we have $\Delta G^{\varphi}_{\text{ext}} = 0$ yielding the identity $\Delta G^{\varphi} \equiv \Delta G^{\varphi}_{\text{int}}$.

Recalling the explicit algorithmic form of G^{ϕ}_{int} from (16), the increment $\Delta G^{\phi}_{\text{int}}$ can be expressed as

$$\Delta G^{\phi}_{\text{int}} = \int_{\mathcal{B}} \delta\Phi\, \frac{\Delta\Phi}{\Delta t} + \Delta(\nabla_x\delta\Phi) \cdot \hat{\boldsymbol{q}} + \nabla_x(\delta\Phi) \cdot \Delta\hat{\boldsymbol{q}} dV. \tag{26}$$

Analogous to (20), linearization of $\nabla_x(\delta\Phi)$ leads to

$$\Delta(\nabla_x(\delta\Phi)) = -\nabla_x(\delta\Phi)\,\nabla_x(\Delta\boldsymbol{\varphi}). \tag{27}$$

Furthermore, based on the functional definition of the spatial potential flux $\hat{\boldsymbol{q}}$ in (8), we obtain

$$\Delta\hat{\boldsymbol{q}} = \pounds_{\Delta\boldsymbol{\varphi}}\hat{\boldsymbol{q}} + \nabla_x(\Delta\boldsymbol{\varphi})\cdot\hat{\boldsymbol{q}} + \hat{\boldsymbol{D}}\cdot\nabla_x(\Delta\Phi) \tag{28}$$

where $\pounds_{\Delta\boldsymbol{\varphi}}\hat{\boldsymbol{q}}$ denotes the Lie derivative of the potential flux $\hat{\boldsymbol{q}}$ along the increment $\Delta\boldsymbol{\varphi}$

$$\pounds_{\Delta\boldsymbol{\varphi}}\hat{\boldsymbol{q}} = \boldsymbol{\mathcal{C}}^{\phi\varphi} : \tfrac{1}{2}\pounds_{\Delta\boldsymbol{\varphi}}\boldsymbol{g} = \boldsymbol{\mathcal{C}}^{\phi\varphi} : (\boldsymbol{g}\nabla_x(\Delta\boldsymbol{\varphi})). \tag{29}$$

In Eqs. (28) and (29), we introduced the second-order deformation-dependent conduction tensor $\hat{\boldsymbol{D}}$ and the third-order mixed moduli $\boldsymbol{\mathcal{C}}^{\phi\varphi}$ that are defined as

$$\hat{\boldsymbol{D}} := \partial_{\nabla_x\Phi}\hat{\boldsymbol{q}}(\boldsymbol{g};\boldsymbol{F},\Phi) \quad\text{and}\quad \boldsymbol{\mathcal{C}}^{\phi\varphi} := 2\partial_{\boldsymbol{g}}\hat{\boldsymbol{q}}(\boldsymbol{g};\boldsymbol{F},\Phi), \tag{30}$$

respectively. Substituting the results (27) and (28) and the definitions (29) and (30) into (26), we end up with

$$\begin{aligned}\Delta G^{\phi}_{\text{int}} = &\int_{\mathcal{B}} \delta\Phi\,\frac{\Delta\Phi}{\Delta t}\,dV \\ &+ \int_{\mathcal{B}} \nabla_x(\delta\Phi)\cdot\hat{\boldsymbol{D}}\cdot\nabla_x(\Delta\Phi)\,dV \\ &+ \int_{\mathcal{B}} \nabla_x(\delta\Phi)\cdot\boldsymbol{\mathcal{C}}^{\phi\varphi} : (\boldsymbol{g}\nabla_x(\Delta\boldsymbol{\varphi}))\,dV.\end{aligned} \tag{31}$$

In contrast to G^{φ}_{ext}, the external term G^{ϕ}_{ext} in (12) depends non-linearly on the field variables through the source term $\hat{F}^{\phi}(\boldsymbol{g};\boldsymbol{F},\Phi)$ introduced in (9). For a given $\bar{q}$ on $\partial\mathcal{S}_q$, we then obtain the following incremental form

$$\Delta G^{\phi}_{\text{ext}} := \int_{\mathcal{B}} \delta\Phi\;\Delta\hat{F}^{\phi}\,dV. \tag{32}$$

In the Eulerian setting, linearization of the scalar-valued function $\hat{F}^{\phi}$ yields

$$\Delta\hat{F}^{\phi} = \boldsymbol{H} : (\boldsymbol{g}\nabla_x(\Delta\boldsymbol{\varphi})) + H\Delta\Phi \tag{33}$$

where the tangent terms $\boldsymbol{H}$ and H are defined as

$$\boldsymbol{H} := 2\partial_{\boldsymbol{g}}\hat{F}^{\phi}(\boldsymbol{g};\boldsymbol{F},\Phi) \quad\text{and}\quad H := \partial_{\Phi}\hat{F}^{\phi}(\boldsymbol{g};\boldsymbol{F},\Phi), \tag{34}$$

respectively. Based on the decomposed form introduced in (9), the scalar tangent term H can be expressed as

$$H = H_{\text{e}} + H_{\text{m}} \quad\text{with}\quad H_{\text{e}} := \partial_{\Phi}\hat{F}^{\phi}_{\text{e}},\quad H_{\text{m}} := \partial_{\Phi}\hat{F}^{\phi}_{\text{m}}. \tag{35}$$

Inserting the results (33) and (34) into (32), we obtain the linearized external term

$$\Delta G^{\phi}_{\text{ext}} = \int_{\mathcal{B}} \delta\Phi\,\left(\boldsymbol{H} : (\boldsymbol{g}\nabla_x(\Delta\boldsymbol{\varphi})) + H\Delta\Phi\right)\,dV. \tag{36}$$

This completes the linearization within the continuous spatial setting. In the subsequent part, we carry out the spatial discretization of the field variables to obtain algebraic counterparts of the residual expressions (13) and (14).

3.3 Spatial discretization

To approximate the continuous integral equations for the weak forms (11) and (12) derived in the preceding section, we follow the conventional isoparametric Galerkin procedure. To this end, we discretize the domain of interest $\mathcal{B}$ into element subdomains $\mathcal{B}^h_e$ such that $\mathcal{B} \approx \mathcal{B}^h = \bigcup_{e=1}^{\text{n}_{\text{el}}} \mathcal{B}^h_e$ with n_{el} denoting the total number of elements. We then interpolate the field variables and the associated weight functions over each element domain by introducing the corresponding discrete nodal values and $\mathcal{C}^0$ shape functions

$$\begin{aligned}\delta\boldsymbol{\varphi}^h_e &= \sum_{i=1}^{\text{n}_{\text{en}}} N^i\,\delta\boldsymbol{x}^e_i, \quad \delta\Phi^h_e = \sum_{j=1}^{\text{n}_{\text{en}}} N^j\,\delta\Phi^e_j, \\ \boldsymbol{\varphi}^h_e &= \sum_{k=1}^{\text{n}_{\text{en}}} N^k\,\boldsymbol{x}^e_k, \quad \Phi^h_e = \sum_{l=1}^{\text{n}_{\text{en}}} N^l\,\Phi^e_l,\end{aligned} \tag{37}$$

where n_{en} refers to the number of nodes per element. Based on the discretization (37), the spatial gradient of the weight functions read as

$$\begin{aligned}\nabla_x(\delta\boldsymbol{\varphi}^h_e) &= \sum_{i=1}^{\text{n}_{\text{en}}} \delta\boldsymbol{x}^e_i \otimes \nabla_x N^i, \\ \nabla_x(\delta\Phi^h_e) &= \sum_{j=1}^{\text{n}_{\text{en}}} \delta\Phi^e_j \otimes \nabla_x N^j.\end{aligned} \tag{38}$$

Likewise, we obtain the spatial gradient of the incremental fields

$$\begin{aligned}\nabla_x(\Delta\boldsymbol{\varphi}^h_e) &= \sum_{k=1}^{\text{n}_{\text{en}}} \Delta\boldsymbol{x}^e_k \otimes \nabla_x N^k, \\ \nabla_x(\Delta\Phi^h_e) &= \sum_{l=1}^{\text{n}_{\text{en}}} \Delta\Phi^e_l \otimes \nabla_x N^l.\end{aligned} \tag{39}$$

Incorporating the discretized representations (37) and (38) in (11) and (12) along with (13) and (14), we end up with the discrete residual vectors

$$\begin{aligned}\boldsymbol{R}^{\varphi}_I = \mathop{\mathsf{A}}_{e=1}^{\text{n}_{\text{el}}} \Bigg\{ &\int_{\mathcal{B}^h_e} \nabla_x N^i \cdot \hat{\boldsymbol{\tau}}\;dV \\ &- \int_{\mathcal{B}^h_e} N^i\,\boldsymbol{B}\;dV - \int_{\partial\mathcal{S}^e_t} N^i\,\bar{\boldsymbol{t}}\;da \Bigg\} = \boldsymbol{0},\end{aligned}$$

$$R_J^{\phi} = \mathsf{A}_{e=1}^{n_{el}} \left\{ \int_{\mathcal{B}_e^h} (N^j \, \frac{\Phi - \Phi_n}{\Delta t} + \nabla_x N^j \cdot \hat{\boldsymbol{q}}) \, dV \right.$$

$$\left. - \int_{\mathcal{B}_e^h} N^j \, \hat{F}^{\phi} \, dV - \int_{\partial \mathcal{S}_q^e} N^j \, \bar{q} \, da \right\} = 0, \tag{40}$$

where the operator A designates the standard assembly of element contributions at the local element nodes $i, j = 1, \ldots, n_{en}$ to the global residuals at the global nodes $I, J = 1, \ldots, n_{nd}$ of a mesh with n_{nd} nodes. Following the analogous steps, the discrete form of the linearized residual terms (17) can readily be obtained by substituting the discretized representations (37) and (39) in (25), (31), and (36). This step, however, is left out for the sake of conciseness.

4 Model problem

In this section, we present specific forms of the constitutive equations that are utilized in the representative numerical examples in Sect. 5. In particular, we identify the concrete expressions for the Kirchhoff stress $\hat{\boldsymbol{\tau}}$, the potential flux $\hat{\boldsymbol{q}}$, and the current source $\hat{F}^{\phi}$, whose functional dependencies have already been briefly outlined in Sect. 2.3. These constitutive equations include not only the explicit functional evaluations but also the accompanying ordinary differential equations governing the temporal evolution of additional internal variables. This, in turn, necessitates construction of algorithmic procedures for the local update of these internal variables at quadrature points. Hence, the tangent moduli introduced in Sect. 3.2 have to be computed consistently with the employed algorithmic integration scheme for the update of internal variables.

4.1 Active and passive stress response

Before going into the details of the model problem, it is crucial to introduce an approach that we devise to account for the fibrous micro-structure of cardiac tissue in the current model. As mentioned in Sect. 1, cardiac tissue possesses a highly anisotropic micro-structure that is chiefly made up of unevenly distributed myofibers. This heterogeneous but well-organized architecture is of fundamental importance for the successful transduction of essentially one-dimensional excitation–contraction of individual cardiac cells to the overall pumping function of the heart. For this reason, the constitutive equations describing the passive and active tissue stress response, as well as the one controlling the conductivity, have to account for the inherently anisotropic micro-structure. It is the objective of this section to demonstrate that an elementary constitutive approach accounting for basic physical features of cardiac tissue can reproduce physiological results. For this purpose, we restrict ourselves to transversely isotropic cardiac tissue with one single, spatially varying preferred direction that characterizes the local orientation of myofibers. Specifically, we let $\boldsymbol{a}_0(\boldsymbol{X}) \in T_X\mathcal{B}$ be a unit vector, i.e. $|\boldsymbol{a}_0|_{\boldsymbol{G}} = 1$, and denote the average preferred direction of myofibers in the reference configuration at a material point $\boldsymbol{X}$. Under the action of $\boldsymbol{\varphi}_t$, this vector is mapped onto its spatial counterpart $\boldsymbol{a}(\boldsymbol{x}) = \boldsymbol{F}\boldsymbol{a}_0 \in T_x\mathcal{S}$ emanating from $\boldsymbol{x} = \boldsymbol{\varphi}_t(\boldsymbol{X})$. Moreover, we define the symmetric reference structural tensor

$$\boldsymbol{M}(\boldsymbol{X}) := \boldsymbol{a}_0 \otimes \boldsymbol{a}_0 \tag{41}$$

as a key measure of the underlying transversely isotropic material symmetry. Structural tensors are widely employed to develop coordinate-free representation of isotropic tensor functions for anisotropic response of materials, see e.g. Spencer [40].

We now assume the following elementary form for the purely mechanical, passive part of the Kirchhoff stress tensor $(7)_1$

$$\hat{\boldsymbol{\tau}}^{\text{pas}}(\boldsymbol{g}; \boldsymbol{F}, \boldsymbol{M}) = \left(\frac{\lambda}{2} \ln I_3 - \mu\right) \boldsymbol{g}^{-1} + \mu \boldsymbol{b} + 2\vartheta \, \eta (I_4 - 1) \boldsymbol{m} \tag{42}$$

in terms of the inverse metric $\boldsymbol{g}^{-1}$, the left Cauchy–Green tensor $\boldsymbol{b} := \boldsymbol{F}\boldsymbol{G}^{-1}\boldsymbol{F}^T$, and the deformed structural tensor $\boldsymbol{m} := \boldsymbol{a} \otimes \boldsymbol{a} = \boldsymbol{F}\boldsymbol{M}\boldsymbol{F}^T$. The Lamé constants λ and μ govern the isotropic stress response, while the parameter η can be conceived as the passive stiffness of myofibers. The anisotropic part of the stress is assumed to be active only when the fibers are under tension. This condition is imposed through the following conditional definition of the coefficient ϑ

$$\vartheta(\bar{\lambda}) = \begin{cases} 1 & \text{if } \bar{\lambda} > 1, \\ 0 & \text{otherwise}, \end{cases} \tag{43}$$

where $\bar{\lambda} := |\boldsymbol{a}|_{\boldsymbol{g}} = \sqrt{\boldsymbol{a} \cdot \boldsymbol{g}\boldsymbol{a}}$ refers to the stretch in the preferred direction $\boldsymbol{a}$. Furthermore, the invariants I_3 and I_4 appearing in the stress expression (42) are defined as

$$I_3 := J^2 = \det(\boldsymbol{F}^T \boldsymbol{g} \boldsymbol{F}) \quad \text{and} \quad I_4 := \boldsymbol{g} : \boldsymbol{m}, \tag{44}$$

respectively. Observe that the invariant I_4 is none other than the fiber stretch squared, $I_4 = \bar{\lambda}^2$.

Since the active Kirchhoff stress $\hat{\boldsymbol{\tau}}^{\text{act}}$ is generated by excitation-induced contraction of spatially well organized cardiac cells, this part of the stress tensor is considered to be of purely anisotropic form

$$\hat{\boldsymbol{\tau}}^{\text{act}}(\boldsymbol{g}; \boldsymbol{F}, \Phi, \boldsymbol{M}) = \sigma(\Phi) \, \boldsymbol{m}. \tag{45}$$

In contrast to recent constitutive equations proposed in the literature, e.g. [22,25], where the active stress contribution is incorporated as an isotropic function, we assume that the

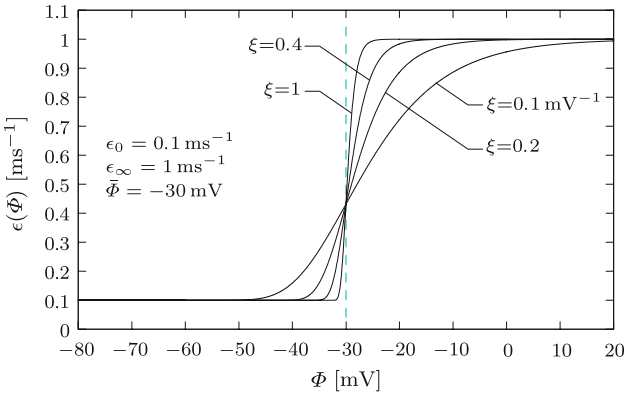

Fig. 3 Switch function $\epsilon(\Phi)$ is plotted against the potential Φ for different values of the rate parameter ξ=0.1, 0.2, 0.4, 1 mV^{-1} and for ϵ_0=0.1 ms^{-1}, ϵ_∞=1 ms^{-1}, $\bar{\Phi}$= − 30 mV

active part is entirely anisotropic. From the geometrical point of view, the active stress expression (45) implies that the direction of the active stress tensor is dictated by the deformed structural tensor $\boldsymbol{m}$, while its magnitude is chiefly determined by the transmembrane potential-dependent active fiber tension $\sigma(\Phi)$. To model the twitch-like response of the fiber tension $\sigma(\Phi)$, we adopt the evolution equation proposed by Nash and Panfilov [22]

$$\dot{\sigma} = \epsilon(\Phi)[k_\sigma(\Phi - \Phi_r) - \sigma]\,, \tag{46}$$

where the parameter k_σ controls the saturated value of σ for a given potential Φ and a given resting potential Φ_r, which is about −80 mV for cardiac cells. That is, $\dot{\sigma}$ vanishes identically when σ admits the value $\sigma_\infty = k_\sigma(\Phi - \Phi_r)$ for $\epsilon(\Phi) \neq 0$. Moreover, contrary to its Heaviside form proposed in [22], we use the following smoothly varying form for the rate switch function

$$\epsilon(\Phi) = \epsilon_0 + (\epsilon_\infty - \epsilon_0)\exp[-\exp(-\xi(\Phi - \bar{\Phi}))] \tag{47}$$

in terms of the parameters ϵ_0 and ϵ_∞ that characterize the two limiting values of the function for $\Phi < \bar{\Phi}$ and $\Phi > \bar{\Phi}$ about the phase shift $\bar{\Phi}$, respectively. In addition, the transition rate of ϵ from ϵ_0 to ϵ_∞ about $\bar{\Phi}$ is determined by the parameter ξ. As depicted in Fig. 3, as the value of ξ gets higher, the transition of the function ϵ from ϵ_0 to ϵ_∞ becomes sharper.

In order to compute the current value of σ, we use the backward Euler scheme. For a typical time step $\Delta t = t - t_n$, we then obtain

$$\sigma = \sigma_n + \Delta t\,\epsilon(\Phi)[k_\sigma(\Phi - \Phi_r) - \sigma]. \tag{48}$$

This immediately results in a closed-form algorithmic expression for the current value of the active fiber tension

$$\sigma(\Phi) = \frac{1}{1 + \Delta t\,\epsilon(\Phi)}\,[\sigma_n + \Delta t\,\epsilon(\Phi)\,k_\sigma(\Phi - \Phi_r)] \tag{49}$$

in terms of the current action potential Φ and σ_n at time t_n that is stored as a history variable at each quadrature point of the finite element model. Having the stress expressions at hand, we are now in a position to determine the moduli based on the definition $(24)_1$

$$\mathbb{C}^{\varphi\varphi} = \lambda\, \boldsymbol{g}^{-1} \otimes \boldsymbol{g}^{-1} - (\lambda\, \ln I_3 - 2\mu)\, \mathbb{I}_{\boldsymbol{g}^{-1}} + 4\vartheta\, \eta\, \boldsymbol{m} \otimes \boldsymbol{m} \tag{50}$$

where we have made use of the results $\partial_{\boldsymbol{g}} I_3 = I_3\, \boldsymbol{g}^{-1}$, $\partial_{\boldsymbol{g}} I_4 = \boldsymbol{m}$. The symmetric fourth identity tensor $\mathbb{I}_{\boldsymbol{g}^{-1}} := -\partial_{\boldsymbol{g}} \boldsymbol{g}^{-1}$ has the indicial representation $\mathbb{I}^{ijkl}_{\boldsymbol{g}^{-1}} := \frac{1}{2}(g^{ik} g^{jl} + g^{il} g^{jk})$ in terms of the components of the inverse metric g^{ij}. Similarly, the sensitivity of the Kirchhoff stress tensor to the transmembrane potential then follows from $(24)_2$

$$\boldsymbol{C}^{\varphi\phi} = \sigma'(\Phi)\, \boldsymbol{m} \quad \text{with} \quad \sigma'(\Phi) := \partial_\Phi \sigma(\Phi). \tag{51}$$

Being consistent with the implicit integration scheme employed in (49), it can be readily shown that

$$\sigma'(\Phi) = \frac{\Delta t}{1 + \Delta t\,\epsilon(\Phi)} \times \left[\epsilon'(\Phi)(k_\sigma(\Phi - \Phi_r) - \sigma) + \epsilon(\Phi)\, k_\sigma\right], \tag{52}$$

where the derivative $\epsilon'(\Phi) := \partial_\Phi \hat{\epsilon}(\Phi)$ can be obtained from the definition (47)

$$\epsilon'(\Phi) = \xi\,(\epsilon(\Phi) - \epsilon_0)\exp[-\xi(\Phi - \bar{\Phi})]. \tag{53}$$

4.2 Spatial potential flux

We have already introduced the spatial potential flux $\hat{\boldsymbol{q}}$ in (8) in terms of the conduction tensor $\boldsymbol{D}$ $(30)_1$, and the potential gradient $\nabla_x \Phi$. In this model problem, the second-order conduction tensor is additively decomposed into the isotropic and anisotropic parts

$$\boldsymbol{D} = d_{\text{iso}}\, \boldsymbol{g}^{-1} + d_{\text{ani}}\, \boldsymbol{m} \tag{54}$$

in terms of the scalar conduction coefficients d_{iso} and d_{ani}, where the latter accounts for the faster conduction along the myofiber directions. Having $\boldsymbol{D}$ specified, we can express the third-order mixed moduli $\boldsymbol{C}^{\phi\varphi}$ based on their definition given in $(30)_2$

$$\boldsymbol{C}^{\phi\varphi} = -2\, d_{\text{iso}} \nabla_x \Phi \cdot \mathbb{I}_{\boldsymbol{g}^{-1}}. \tag{55}$$

4.3 Current source

In order to complete the description of the model problem, we finally need to specify the constitutive equations for the electrical source term $\hat{F}^\phi$. In the field of phenomenological electrophysiology, it is common practice to set up the model equations and parameters in the non-dimensional space. For this purpose, we introduce the non-dimensional transmembrane potential ϕ and the non-dimensional time τ through

the following conversion formulae

$$\Phi = \beta_\phi \phi - \delta_\phi \quad \text{and} \quad t = \beta_t \tau. \tag{56}$$

The non-dimensional potential ϕ is related to the physical transmembrane potential Φ through the factor β_ϕ and the potential difference δ_ϕ, which are both in millivolt (mV). Likewise, the dimensionless time τ is converted to the physical time t by multiplying it with the factor β_t in millisecond (ms). Having the basic relations (56) at hand, we obtain the following conversion expressions

$$\hat{F}^\phi = \frac{\beta_\phi}{\beta_t}\hat{f}^\phi, \quad \boldsymbol{H} = \frac{\beta_\phi}{\beta_t}\boldsymbol{h} \quad \text{and} \quad H = \frac{1}{\beta_t}h \tag{57}$$

for the normalized source term $\hat{f}^\phi$, and the non-dimensional counterparts $h := \partial_\phi \hat{f}^\phi$ and $\boldsymbol{h} := 2\partial_{\boldsymbol{g}} \hat{f}^\phi$ of the tangent terms defined in (34). The additive split of $\hat{F}^\phi$, introduced in (9) Sect. 2.3, along with $(57)_1$ implies the equivalent decomposition of $\hat{f}^\phi = \hat{f}^\phi_{\mathrm{e}} + \hat{f}^\phi_{\mathrm{m}}$ into the purely electrical part $\hat{f}^\phi_{\mathrm{e}}$ and the stretch-induced mechano-electrical part $\hat{f}^\phi_{\mathrm{m}}$. This also leads to the dimensionless counterpart of (35)

$$h = h_{\mathrm{e}} + h_{\mathrm{m}} \quad \text{with} \quad h_{\mathrm{e}} := \partial_\phi \hat{f}^\phi_{\mathrm{e}}, \; h_{\mathrm{m}} := \partial_\phi \hat{f}^\phi_{\mathrm{m}}. \tag{58}$$

In this model problem, we use the celebrated Aliev–Panfilov model, which favorably captures the characteristic shape of the action potential in excitable ventricular cells,

$$\hat{f}^\phi_{\mathrm{e}} = c\phi(\phi - \alpha)(1 - \phi) - r\,\phi \tag{59}$$

where c, α are material parameters. The evolution of the recovery variable r is governed by the ordinary differential equation (10) through the specific source term

$$\hat{f}^r = \left[\gamma + \frac{\mu_1 r}{\mu_2 + \phi}\right][-r - c\,\phi\,(\phi - b - 1)]. \tag{60}$$

The coefficient term $[\gamma + \mu_1 r/\mu_2 + \phi]$ plays a key role in controlling the restitution characteristics of the model through the additional material parameters μ_1, μ_2, b and γ. The phase diagram in Fig. 4 (top) depicts the solution trajectories of the local ordinary differential equations $\partial_\tau \phi = \hat{f}^\phi_{\mathrm{e}}$ and $\partial_\tau r = \hat{f}^r$ corresponding to different initial points ϕ_0 and r_0. Note that the dashed nullclines, where $\hat{f}^\phi = 0$ or $\hat{f}^r = 0$ vanish, guide the trajectories. The diagrams in Fig. 4 (bottom) show the non-dimensional potential ϕ and the recovery variable r curves plotted against the dimensionless time τ. The action potential is generated by adding external stimulation $I = 30$ to the right-hand side of $\partial_\tau \phi = \hat{f}^\phi_{\mathrm{e}}$ from $\tau = 30$ to $\tau = 30.02$.

Analogous to the algorithmic update of σ, we use the backward Euler integration to calculate the current value of r. Owing to the highly non-linear form of the source $\hat{f}^r$, however, we need to introduce the residual

$$R^r = r - r_n - \Delta\tau\, \hat{f}^r(\phi, r) \doteq 0 \tag{61}$$

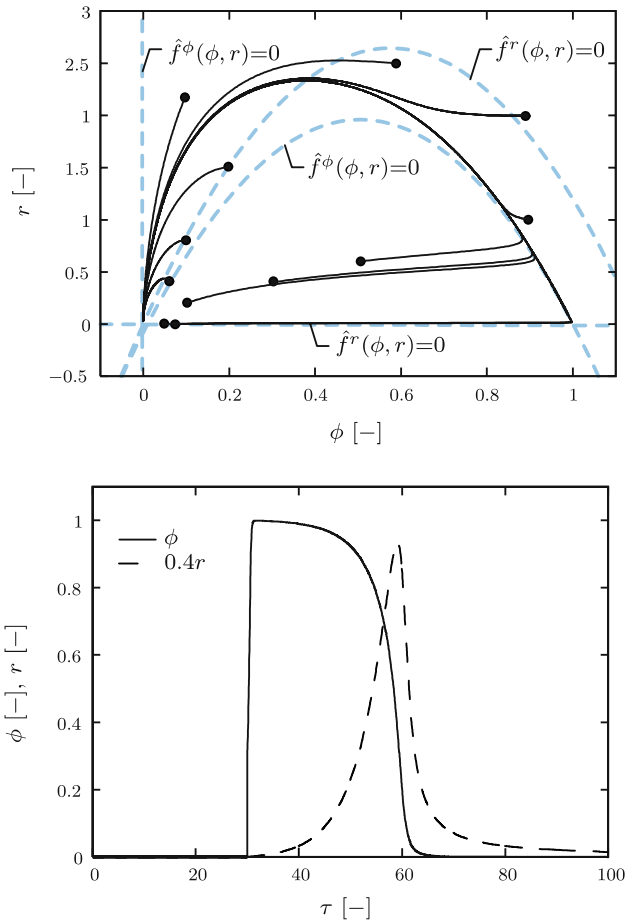

Fig. 4 The Aliev–Panfilov model with $\alpha = 0.01, \gamma = 0.002$, $b = 0.15, c = 8, \mu_1 = 0.2, \mu_2 = 0.3$. The phase portrait depicts trajectories for distinct initial values ϕ_0 and r_0 (*filled circles*) converging to a stable equilibrium point (*top*). Non-oscillatory normalized time plot of the non-dimensional action potential ϕ and the recovery variable r (*bottom*)

that has to be solved iteratively. Linearization of (61) leads us to the local update equation of the recovery variable r

$$r \leftarrow r - (C^{rr})^{-1} R^r, \tag{62}$$

where the scalar local tangent C^{rr} is defined by

$$C^{rr} := \partial_r R^r = 1 + \Delta\tau\left[\gamma + \frac{\mu_1}{\mu_2 + \phi}[2r + c\phi(\phi - b - 1)]\right]. \tag{63}$$

Calculation of the modulus h_e, defined in $(58)_2$, necessitates the knowledge of the derivative of the recovery variable r with respect to the action potential ϕ. This derivative can be calculated based on the persistency condition $\mathrm{d}_\phi R^r = \partial_\phi R^r + \partial_r R^r\, \mathrm{d}_\phi r \doteq 0$, which implies the consistent fulfillment of (61) throughout the whole calculation. Solving this equality for the sought derivative, we obtain $\mathrm{d}_\phi r =$

Table 1 Local Newton update of the internal variable r

Given are r_n and Φ
(i) Calculate $\phi = (\Phi + \delta_\phi)/\beta_\phi$ $(56)_1$
(ii) Set $r \leftarrow r_n$
(iii) Compute R^r (61) and C^{rr} (63)
(iv) Update recovery $r \leftarrow r - (C^{rr})^{-1} R^r$
(v) Check if $|R^r| <$ tol, if no goto (iii), continue otherwise
(vi) Update history for r_n
(vii) Compute $C^{r\phi}$ and $\mathrm{d}_\phi r$ (64)
(viii) Compute $\hat{f}_{\mathrm{e}}^{\phi}$ (59) and h_{e} $(58)_2$

$-(C^{rr})^{-1}\, C^{r\phi}$, where $C^{r\phi}$ is defined and obtained as

$$
\begin{aligned}
C^{r\phi} &:= \partial_\phi R^r \\
&= \Delta\tau \left[[\gamma + \frac{\mu_1 r}{\mu_2 + \phi}]\, c\,(2\phi - b - 1) \right. \\
&\quad \left. - \frac{\mu_1 r}{[\mu_2 + \phi]^2}\, [\, r + c\,\phi\,(\phi - b - 1)\,] \right].
\end{aligned} \tag{64}
$$

With this result at hand, we can obtain the tangent modulus

$$
h_{\mathrm{e}} = c \left[-3\phi^2 + 2[1+\alpha]\,\phi + \alpha \right] - r - \phi \mathrm{d}_\phi r, \tag{65}
$$

and convert it into its physical counterpart $H_{\mathrm{e}} = h_{\mathrm{e}}/\beta_t$ by using $(57)_3$. We summarize the local Newton iteration for the update of the internal variable r and subsequent computation of the corresponding source term $\hat{f}_{\mathrm{e}}^{\phi}$ and its linearization $\mathrm{d}_\phi f^\phi$ in Table 1.

For the stretch-induced current generation $\hat{f}_{\mathrm{m}}^{\phi}$, we adopt the formula proposed by Panfilov, Keldermann and Nash [13, 29]

$$
\hat{f}_{\mathrm{m}}^{\phi} = \vartheta\, G_s (\bar{\lambda} - 1)(\phi_{\mathrm{s}} - \phi) \tag{66}
$$

where G_s and ϕ_s denote the maximum conductance and the resting potential of the stretch-activated channels, separately. This contribution to the current source term is due to the opening of ion channels, and therefore, exists only when myofibers are under tension. This condition is enforced through the coefficient ϑ defined in (43). With (66) at hand, the tangent terms h_{m}, $\boldsymbol{h}$ can be immediately obtained as

$$
h_{\mathrm{m}} = \vartheta\, G_s (\bar{\lambda} - 1) \quad \text{and} \quad \boldsymbol{h} = \vartheta\, G_s (\phi - \phi_s) \bar{\lambda}^{-1} \boldsymbol{m}\,, \tag{67}
$$

and converted to their counterparts H_{m} and $\boldsymbol{H}$ (35) and (34), through the conversion rules given in (57).

Having the specific expressions for the constitutive equations introduced and their algorithmic treatment elaborated, we can now implement the model problem in a finite element code according to the formulation outlined in Sect. 3. The basic steps of the algorithmic implementation of the model problem are briefly summarized in Table 2 where Table 1 is implicitly embodied in Step v. In addition, the material parameters of the specified model problem are listed in Table 3 along with their brief description and the equation numbers where they appear.

Table 2 Overall algorithmic setting of the model problem

Given are $\boldsymbol{F} = \nabla_X \boldsymbol{\varphi}_t$, Φ, $\nabla_X \Phi$ and history $\mathcal{H} = \{\sigma_n, r_n\}$
(i) Calculate $\boldsymbol{m} = \boldsymbol{F}\boldsymbol{M}\boldsymbol{F}^T$ and $\bar{\lambda} := \sqrt{\boldsymbol{m} : \boldsymbol{g}}$
(ii) Set $\vartheta = 1$ if $\bar{\lambda} \geq 1$; $\vartheta = 0$ otherwise
(iii) Calculate $\hat{\boldsymbol{\tau}}^{\mathrm{pas}}$ (42) and $\mathbb{C}^{\varphi\varphi}$ (50)
(iv) Compute $\phi = (\Phi + \delta_\phi)/\beta_\phi$ and $\Delta\tau = \Delta t/\beta_t$ (56)
(v) Update the recovery variable r based on Table 1
(vi) Compute $\hat{f}_{\mathrm{e}}^{\phi}$ (59), h_{e} (65), h_{m} $(67)_1$ and $\boldsymbol{h}$ $(67)_2$
(vii) Perform conversion to $\hat{F}_{\mathrm{e}}^{\phi}$, H_{m}, H_{e} and $\boldsymbol{H}$ (57)
(viii) Update $\sigma(\Phi)$ (49) and compute $\sigma'(\Phi)$ (52)
(ix) Compute $\hat{\boldsymbol{\tau}}^{\mathrm{act}}$ (45) and $\boldsymbol{C}^{\varphi\phi}$ (51)
(x) Calculate $\hat{\boldsymbol{q}}$ (8), $\boldsymbol{D}$ (54) and $\boldsymbol{\mathcal{C}}^{\phi\varphi}$ (54)

Table 3 Material parameters of the specified model

Parameter	Description	Equation
$\lambda,\ \mu$	Lamé constants	(42)
η	Passive stiffness of myofibers	(42)
k_σ	Saturated active stress	(46)
Φ_r	Resting potential	(46)
$\epsilon_0, \epsilon_\infty$	Rate constants of contraction (Fig. 3)	(47)
$\xi, \bar{\Phi}$	Transition rate and phase shift (Fig. 3)	(47)
$d_{\mathrm{iso}}, d_{\mathrm{ani}}$	Conduction speed	(54)
α, b, c	Dynamics of the AP-model (Fig. 4)	(59) and (60)
γ, μ_1, μ_2	Restitution properties (Fig. 4)	(59) and (60)
G_s, ϕ_s	Stretch-induced excitation	(66)
$[\beta_\phi, \delta_\phi, \beta_t$	Conversion factors	(56)]

Table 4 Values of the material parameters used in analyses

Passive stress	$\lambda = 0.5$ MPa, $\mu = 0.2$ MPa, $\eta = 0.1$ MPa
Active stress	$k_\sigma = 0.005$ MPa mV^{-1}, $\Phi_r = -80$ mV
Switch function	$\Phi_r = -80$ mV, $\epsilon_0 = 0.1$ mV^{-1}, $\epsilon_\infty = 1$ mV^{-1}
	$\xi = 1$ mV^{-1}, $\bar{\Phi} = 0$ mV
Conduction	$d_{\mathrm{iso}} = 1$ mm^2 ms^{-1}, $d_{\mathrm{ani}} = 0.1$ mm^2 ms^{-1}
Excitation	$\alpha = 0.01[-]$, $b = 0.15[-]$, $c = 8[-]$
	$\gamma = 0.002[-]$, $\mu_1 = 0.2[-]$, $\mu_2 = 0.3[-]$
	$G_s = 10[-]$, $\phi_s = 0.6[-]$

5 Representative numerical examples

This section is devoted to the illustrative numerical examples chosen to demonstrate the key features and capabilities of the proposed formulation. With this aim in mind, we consider three initial boundary-value problems. First, we illustrate the mechano-electric feedback on a slice of cardiac tissue whose center is subjected to impact loading. The second example is concerned with the formation and stable rotation of scroll waves in excitable and deformable cardiac tissue. This phenomenon is closely related to re-entrant cardiac arrhythmias, and thus to atrial and ventricular fibrillation. Lastly, we present a coupled electromechanical analysis of a biventricular generic heart model that successfully demonstrates the main physiological features of the overall response of the heart.

Unless stated otherwise, we used the values of the material parameters given in Table 4 in the finite element analyses

of the examples presented in this section. Observe that the parameters belonging to the Aliev–Panfilov model $\hat{f}_{\mathrm{e}}^{\phi}$ and to the stretch-induced part of the excitation source $\hat{f}_{\mathrm{m}}^{\phi}$ are dimensionless. This is consistent with the non-dimensional setting introduced through the conversion formulae (56) and (57). In the conversion, we employ the factors $\beta_\phi = 100$ mV, $\delta_\phi = -80$ mV and $\beta_t = 12.9$ ms that are chosen to obtain the physiological action potential response ranging from −80 to +20 mV and the characteristic action potential duration, as suggested in [1].

5.1 Deformation-induced excitation of cardiac tissue

In order to illustrate the phenomenon of mechano-electric feedback, we consider a three-dimensional 100mm × 100mm × 12 mm slice of cardiac tissue, see the upper leftmost panel in Fig. 6 for dimensioning. The tissue block is discretized into 21×21×2 eight-node coupled brick elements. The myofibers are assumed to be oriented in $x-$direction, i.e. $\boldsymbol{a}_0 = \boldsymbol{e}_1$, with respect to the global coordinate system depicted in Fig. 5. Initial value of the transmembrane potential in the whole domain is set to its resting value $\Phi(\boldsymbol{X}, t_0) = -80$ mV. The displacement degrees of freedom in the z-direction at the nodes located on the four edges of the mid-plane ($z = 6$) of the slice are restrained. Moreover, the displacements in the x- and y-directions at $(0, 0, 0)$ and the displacement in the y-direction at the node located at $(100, 0, 0)$ are fixed. Furthermore, the outer surface of the tissue is assumed to be electrically insulated, i.e. $\bar{q} = 0$ on $\partial\mathcal{S}$. In order to initiate the excitation, the nodes located within the central, 20 mm × 20 mm × 12 mm, parallelepiped are subjected to impulsive cyclic loading $\bar{p}(t)$ in z-direction, see the upper leftmost panel Fig. 5. The loading $\bar{p}(t)$ is increased proportionally up to 1 N within the first 5 ms and then decreased back to the zero load level at the same rate. The snapshot taken at $t = 5$ ms in Fig. 5 demonstrates the deformed shape of the tissue at the instant of peak loading. Besides the deformed shapes, the contour plots of action potential are also depicted at each snapshot.

The impulsive loading in the transverse direction gives rise to the tension-dominated deformation in the center of the tissue. This region then undergoes the stretch-induced excitation through the activation of ion channels due to the source term $\hat{F}_{\mathrm{m}}^{\phi}$ introduced in (9) and (66) as depicted in the panel at $t = 10$ ms in Fig. 5. The excitation leads to depolarization of the tissue from the center, and in turn, exci-

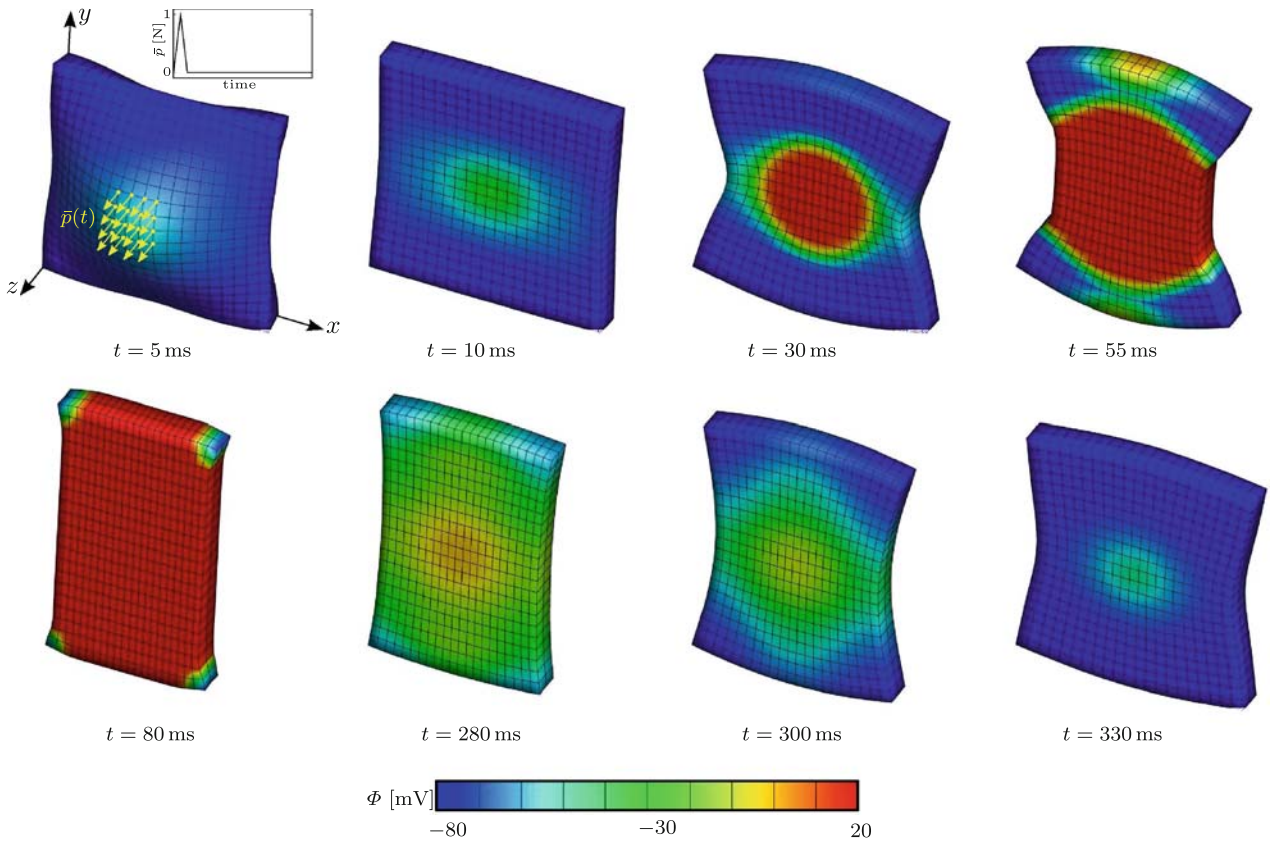

Fig. 5 Deformation-induced excitation of deformable cardiac tissue. Snapshots of the deformed model depict the action potential contours at different stages of depolarization (*upper row*) and repolarization (*lower row*). Note that the cardiac tissue recovers its original shape at $t = 0$ ms upon completion of repolarization at $t \approx 360$ ms

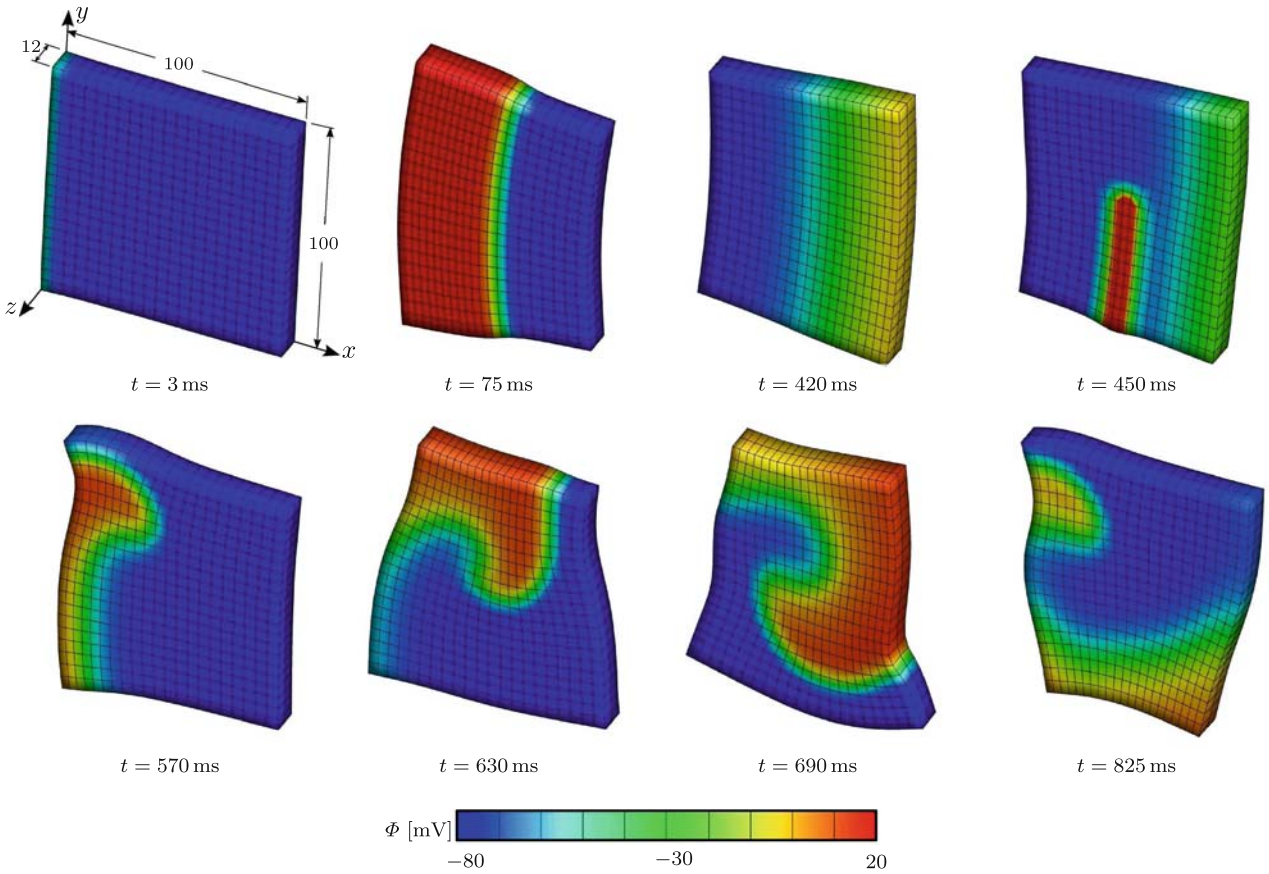

Fig. 6 Initiation and rotation of scroll re-entry in excitable and deformable cardiac tissue. The re-entrant scroll is triggered by externally stimulating tail of the repolarization wave through the addition of $I = 5$ to $\hat{f}_{\mathrm{e}}^{\phi}$ from 440 to 460 ms at the rectangular region

tation-induced contraction of myofibers that are located in the x-direction, see the snapshot at $t = 30$ ms. Both the contraction of myofibers and the higher rate of conduction in the x-direction result in faster depolarization along that direction. This non-uniform deformation pattern brings about the bending of the slice, thereby triggering secondary excitation at the upper and lower edges of the domain, as shown in the panel corresponding to $t = 55$ ms. The two depolarization fronts then merge, and cause the whole tissue to become completely depolarized, see the panel at $t = 80$ ms. The snapshots taken at $t = 280, 300, 330$ ms illustrate the sequence of tissue repolarization from the excited state with $\Phi = +20$ mV back to the resting state with $\Phi = -80$ mV. The repolarization process is also accompanied by the relaxation of myocytes leading to the recovery of the original shape at around $t = 360$ ms.

5.2 Scroll waves in a slice of cardiac tissue

One of the key benchmark problems of computational cardiac electrophysiology and electromechanics is the simulation of three-dimensional scroll waves. These re-entrant waves are closely related to cardiac arrhythmias, such as atrial and ventricular fibrillation. Re-entry may arise from different inhomogeneities such as the uneven distribution of conduction properties in diseased tissue as in the case of unidirectional block or unsynchronized multiple pacemakers.

In order to simulate the re-entrant waves in deformable cardiac tissue, we devise the same geometry and discretization as the one used in the preceding boundary-value problem, see the panel at $t = 3$ ms in Fig. 6. The values of the material parameters are selected to be the same as in Table 4 except that $G_s = 0$ such that mechano-electric feedback effect is suppressed. To generate a scroll wave, we follow the conventional procedure suggested in [8,9]. To this end, we initiate a planar depolarization front in x-direction by assigning elevated initial values to the nodal action potentials $\Phi_0 = -40$ mV on the plane located at $x = 0$ mm. The initial value of the nodal transmembrane potential at the remainder of the nodes is set to the resting value $\Phi_0 = -80$ mV. The outer surface of the tissue is assumed to be electrically flux-free. Moreover, the orientation of contractile myofibers is assumed to be $\boldsymbol{a}_0 = \boldsymbol{e}_1$ with respect to the global coordinate system depicted in Fig. 6. In contrast to the mechanical essential boundary conditions utilized in the preceding example, no degree of freedom is a priori prescribed here.

Instead, the nodes on the plane situated at $z = 0$ are supported by uncoupled linear springs of directional stiffnesses $k_x = k_y = 10^{-3}$ N/mm and $k_z = 10^{-1}$ N/mm. This has resulted in a system of equations that is stable enough to tackle, while at the same time, providing a fairly unconstrained representation of deformed configurations.

Once the wave front has formed, it starts to travel in x-direction, thereby depolarizing the whole domain and leading to contraction of myocytes, see the panel at $t = 75$ ms in Fig. 6. The myocytes then start to relax in the region where the repolarization tail has taken over, as shown in the snapshot at $t = 420$ ms. To initiate the spiral wave re-entry, we externally stimulate the rectangular region bounded by the coordinates $x \in [40, 50]$ mm, $y \in [0, 55]$ mm and $z \in [0, 12]$ mm with respect to the initial configuration. The rectangular region is depolarized by adding the extra current $I = 5$ to $\hat{f}_e^{\phi}$ at time $t = 440$ ms for 20 ms. Observe that the snapshots corresponding to the time steps following the stimulation clearly demonstrate the stages of initiation, development, and stable rotation of the scroll wave re-entry.

It is important to note that, contrary to the purely electrophysiology-based simulations of re-entrant waves on regular domains, the center of the scroll does not remain stationary but drifts due to the deformation, see also [30]. Another crucial observation concerns the substantial reduction of the action potential duration once the scroll wave is initiated. This is closely related to the restitution property of cardiac cells that are able to adjust the action potential duration adaptively depending upon the frequency of excitation. This feature is well captured by the Aliev–Panfilov model through the non-linear coefficient term in (60) as discussed extensively in [1,8].

5.3 Excitation–contraction of a generic heart model

The key motivation for this work is its potential application in guiding stem cell-based therapies in heart failure. As a first attempt towards this objective, we carry out a three-dimensional coupled electromechanical analysis of a biventricular generic heart model and show that basic features of the heart function can be captured by our model. The solid model of a biventricular generic heart is constructed by means of two truncated ellipsoids as suggested in [39]. The generic heart model whose dimensions and spatial discretization are depicted in Fig. 7 is meshed with 13,348 four-node coupled tetrahedral elements connected at 3,059 nodes. The unevenly distributed average orientation of contractile myocytes $\boldsymbol{a}_0$ is depicted with yellow lines in Fig. 8. This fiber organization is consistent with the myofiber orientation in the human heart where the fiber angle ranges from approximately $-70°$ in the epicardium to $+70°$ in the endocardium with respect to the z-plane. Displacement degrees of freedom on the top base surface ($z = 0$) are restrained and the whole surface of

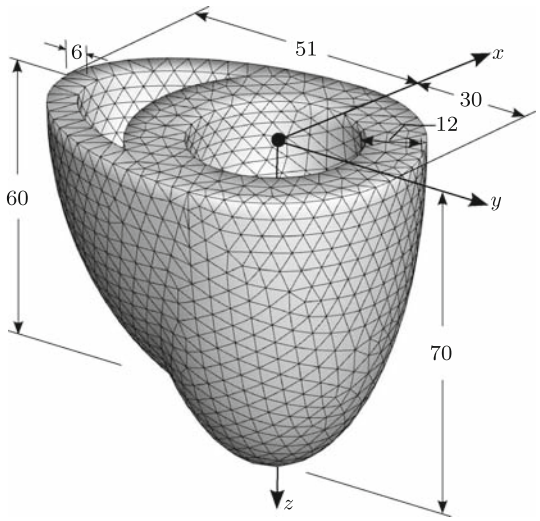

Fig. 7 Geometry and discretization of a generic heart model generated by truncated ellipsoids. Dimensions are in millimeters

the heart is assumed to be flux-free. Moreover, we use the same values of the material parameters as in the preceding example.

To initiate the excitation, the elevated initial value $\Phi_0 = -10$ mV of the transmembrane potential is assigned to the nodes located at the upper part of the septum (wall separating the ventricles) as indicated by the partially depolarized region in the panel at $t = 3$ ms in Fig. 8. The initial transmembrane potential at the remaining nodes is set to the resting value $\Phi_0 = -80$ mV. The excitation at the top of the septum generates the depolarization front travelling from the location of stimulation throughout the entire heart, thereby resulting in the contraction of the myocytes, see the snapshots taken at $t = 75, 105, 135$ ms in Fig. 8. At first glance, we observe that the contraction of myocytes gives rise to the upward motion of the apex (bottom part of the heart). More importantly, we also note that the upward motion of the apex is accompanied by the physiologically observed wall thickening and the overall torsional motion of the heart. These effects can be better appreciated by looking at the deformation of the two slices presented in the complementary images shown in Fig. 9. Undoubtedly, it is the inhomogeneous distribution of myocyte orientation, which is incorporated in the model both spatially over the surfaces and across the transmural direction of the ventricular walls, that yields this physiological response through the non-uniform contraction of myofibers. The panels in the lower rows of Figs. 8 and 9 depict the relaxation of the heart during the course of repolarization. At the end of the repolarization process, the reference configuration of the heart is fully recovered. Note that the repolarization starts from regions which depolarized last. This is in accordance with the uneven action potential duration distribution throughout the myocardium where the

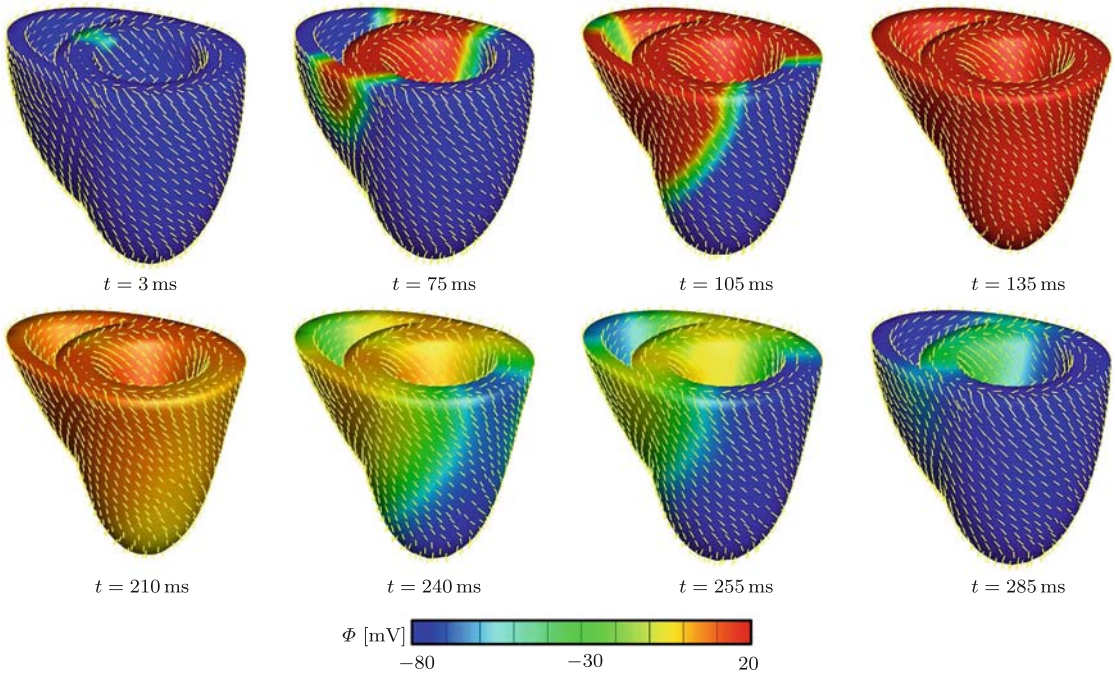

Fig. 8 Coupled excitation-induced contraction of generic heart model. Snapshots of the deformed model depict the action potential contours at different stages of depolarization (*upper row*) and repolarization (*lower row*). The *lines* denote the spatial orientation $\boldsymbol{a}$ of contractile myofibers

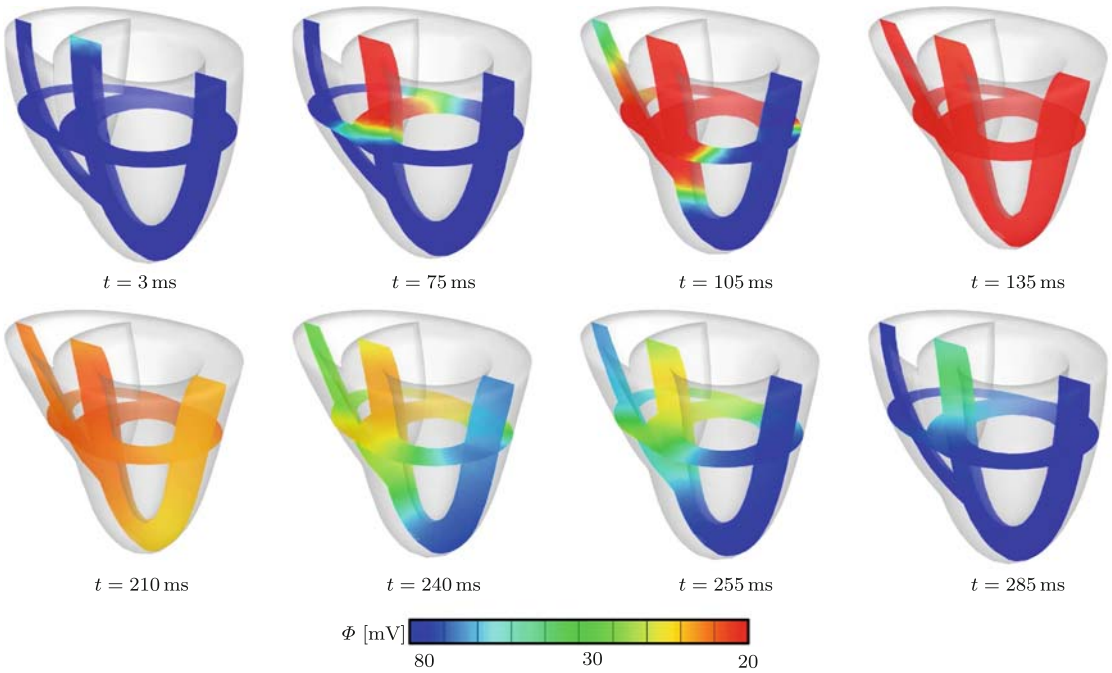

Fig. 9 Coupled excitation-induced contraction of the generic heart model. Snapshots of two slices located at $x = 0$ and $z = 25$ mm (Fig. 7) in the three-dimensional model favorably illustrate the physiological wall thickening and overall torsional motion of the heart at different stages of depolarization (*upper row*) and repolarization (*lower row*)

action potential lasts longer in the endocardial cells than in the epicardial cells [19]. In the present model, this is achieved by altering the temporal converting factor β_t inversely proportional to the excitation time as originally proposed in our recent work on computational modeling of electrocardiograms [17].

6 Concluding remarks

In this manuscript, we have proposed a new, fully implicit, entirely finite element-based numerical approach to the strongly coupled non-linear problem of cardiac electromechanics. The suggested unified algorithmic formulation has been thoroughly set out by giving full particulars of the weak formulation, consistent linearization, and discretization. This has resulted in an unconditionally stable scheme and a modular framework that can readily be extended towards more detailed constitutive approaches. The particular constitutive model considered in this paper accounts for a two-way coupling; that is, both the excitation-induced contraction of cardiac tissue and the deformation-induced generation of excitation have been incorporated. Apart from the intrinsic coupling, the inherent anisotropic micro-structure of cardiac tissue is reflected in the model by means of the modern notions of coordinate-free representation of anisotropy in terms of structural tensors. This concerns not only the passive and active non-linear stress response but also the deformation-dependent conduction tensor. The outstanding performance of the proposed approach has been then demonstrated by means of the three-dimensional benchmark problems that include the re-entrant scroll dynamics and impact loading-generated excitation in the contractile cardiac tissue and the complete coupled electromechanical analysis of a biventricular generic heart model. It is important to emphasize that the fully implicit unified finite element setting allowed us to carry out the benchmark computations with a considerably less computational effort compared to the calculations reported in the literature, which require much finer temporal and spatial discretization.

Acknowledgments This material is based on work supported by the National Science Foundation under Grant No. EFRI-CBE 0735551 Engineering of cardiovascular cellular interfaces and tissue constructs.

References

1. Aliev RR, Panfilov AV (1996) A simple two-variable model of cardiac excitation. Chaos, Solitons Fractals 7:293–301
2. Beeler GW, Reuter H (1977) Reconstruction of the action potential of ventricular myocardial fibres. J Physiol 268:177–210
3. Bers DM (2002) Cardiac excitationcontraction coupling. Nature 415:198–205
4. Clayton RH, Panfilov AV (2008) A guide to modelling cardiac electrical activity in anatomically detailed ventricles. Progr Biophys Mol Biol 96:19–43
5. Fenton F, Karma A (1998) Vortex dynamics in three-dimensional continuous myocardium with fiber rotation: filament instability and fibrillation. Chaos Interdiscipl J Nonlinear Sci 8:20–27
6. Fenton FH, Cherry EM, Hastings HM, Evans SJ (2002) Multiple mechanisms of spiral wave breakup in a model of cardiac electrical activity. Chaos Interdiscipl J Nonlinear Sci 12:852–892
7. Fitzhugh R (1961) Impulses and physiological states in theoretical models of nerve induction. Biophys J 1:455–466
8. Göktepe S, Kuhl E (2009) Computational modeling of cardiac electrophysiology: A novel finite element approach. Int J Numer Methods Eng 79:156–178
9. Göktepe S, Wong J, Kuhl E (2009) Atrial and ventricular fibrillation—computational simulation of spiral waves in cardiac tissue. Arch Appl Mech. doi:10.1007/s00419-009-0384-0
10. Hodgkin A, Huxley A (1952) A quantitative description of membrane current and its application to excitation and conduction in nerve. J Physiol 117:500–544
11. Holzapfel GA, Ogden RW (2009) Constitutive modelling of passive myocardium: a structurally based framework for material characterization. Phil Trans Ser A, Math Phys Eng Sci 367(1902):3445–3475. PMID: 19657007
12. Keener JP, Sneyd J (1998) Mathematical physiology. Springer, New York
13. Keldermann R, Nash M, Panfilov A (2007) Pacemakers in a reaction–diffusion mechanics system. J Stat Phys 128:375–392
14. Kerckhoffs R, Healy S, Usyk T, McCulloch A (2006) Computational methods for cardiac electromechanics. Proc IEEE 94: 769–783
15. Klabunde RE (2005) Cardiovascular physiology concepts. Lippincott Williams & Wilkins, Philadelphia
16. Kohl P, Hunter P, Noble D (1999) Stretch-induced changes in heart rate and rhythm: Clinical observations, experiments and mathematical models. Progr Biophys Mol Biol 71:91–138
17. Kotikanyadanam M, Göktepe S, Kuhl E (2009) Computational modeling of electrocardiograms: a finite element approach towards cardiac excitation. Commun Numer Methods Eng. doi:10.1002/cnm.1273
18. Luo CH, Rudy Y (1991) A model of the ventricular cardiac action potential. depolarization, repolarization, and their interaction. Circ Res 68:1501–1526
19. Malmivuo J, Plonsey R (1995) Bioelectromagnetism. Oxford University Press, Oxford
20. Nagumo J, Arimoto S, Yoshizawa S (1962) An active pulse transmission line simulating nerve axon. Proc IRE 50:2061–2070
21. Nash MP, Hunter PJ (2000) Computational mechanics of the heart from tissue structure to ventricular function. J Elast 61:113–141
22. Nash MP, Panfilov AV (2004) Electromechanical model of excitable tissue to study reentrant cardiac arrhythmias. Progr Biophys Mol Biol 85:501–522
23. Nickerson D, Nash M, Nielsen P, Smith N, Hunter P (2006) Computational multiscale modeling in the IUPS physiome project: modeling cardiac electromechanics. IBM J Res Dev 50:617–630
24. Nickerson D, Smith N, Hunter P (2005) New developments in a strongly coupled cardiac electromechanical model. Europace 7:S118–127
25. Niederer SA, Smith NP (2008) An improved numerical method for strong coupling of excitation and contraction models in the heart. Progr Biophys Mol Biol 96:90–111
26. Nielsen PM, Grice IJL, Smaill BH, Hunter PJ (1991) Mathematical model of geometry and fibrous structure of the heart. Am J Physiol 260:H1365–1378
27. Noble D (1962) A modification of the Hodgkin–Huxley equations applicable to purkinje fibre action and pacemaker potentials. J Physiol 160:317–352
28. Opie LH (2004) Heart physiology: from cell to circulation. Lippincott Williams & Wilkins, Philadelphia
29. Panfilov AV, Keldermann RH, Nash MP (2005) Self-organized pacemakers in a coupled reaction-diffusion-mechanics system. Phys Rev Lett 95:258,104–1–258,014–4. PMID: 16384515
30. Panfilov AV, Keldermann RH, Nash MP (2007) Drift and breakup of spiral waves in reaction diffusion mechanics systems. Proc Natl Acad Sci 104:7922–7926
31. Plank G, Burton RA, Hales P, Bishop M, Mansoori T, Bernabeu MO, Garny A, Prassl AJ, Bollensdorff C, Mason F, Mahmood F,

Rodriguez B, Grau V, Schneider JE, Gavaghan D, Kohl P (2009) Generation of histo-anatomically representative models of the individual heart: tools and application. Phil Trans R Soc A 367:2257–2292
32. Pope AJ, Sands GB, Smaill BH, LeGrice IJ (2008) Three-dimensional transmural organization of perimysial collagen in the heart. Am J Physiol Heart Circ Physiol 295(3):H1243–1252
33. Pullan AJ, Buist ML, Cheng LK (2005) Mathematical modeling the electrical activity of the heart. World Scientific, Singapore
34. Rogers JM (2002) Wave front fragmentation due to ventricular geometry in a model of the rabbit heart. Chaos (Woodbury, N.Y.) 12:779–787. PMID: 12779606
35. Rogers JM, McCulloch AD (1994) Nonuniform muscle fiber orientation causes spiral wave drift in a finite element model of cardiac action potential propagation. J Cardiovasc Electrophysiol 5:496–509
36. Rohmer D, Sitek A, Gullberg GT (2007) Reconstruction and visualization of fiber and laminar structure in the normal human heart from ex vivo diffusion tensor magnetic resonance imaging (DTMRI) data. Invest Radiol 42:777–789
37. Sachse FB (2004) Computational cardiology: modeling of Anatomy, electrophysiology, and mechanics. Springer, Berlin
38. Sainte-Marie J, Chapelle D, Cimrman R, Sorine M (2006) Modeling and estimation of the cardiac electromechanical activity. Comput Struct 84:1743–1759
39. Sermesant M, Rhode K, Sanchez-Ortiz G, Camara O, Andriantsimiavona R, Hegde S, Rueckert D, Lambiase P, Bucknall C, Rosenthal E, Delingette H, Hill D, Ayache N, Razavi R (2005) Simulation of cardiac pathologies using an electromechanical biventricular model and XMR interventional imaging. Med Image Anal 9:467–480
40. Spencer AJM (1971) Theory of invariants. In: Eringen A (ed) Continuum Physics, vol 1. Academic Press, New York
41. Tusscher KHWJT, Panfilov AV (2008) Modelling of the ventricular conduction system. Progr Biophys Mol Biol 96:152–170
42. Usyk TP, LeGrice IJ, McCulloch AD (2002) Computational model of three-dimensional cardiac electromechanics. Comput Vis Sci 4:249–257
43. Yin FC, Chan CC, Judd RM (1996) Compressibility of perfused passive myocardium. Am J Physiol Heart Circ Physiol 271(5):H1864–1870
44. Zheng Z, Croft J, Giles W, Mensah G (2001) Sudden cardiac death in the United States. Circulation 104:2158–2163